Control and Parameter Identification of a Permanent Magnet Synchronous Motor with a LC-Filter

Master's Thesis

Anders Roland Pedersen
Department of Energy Technology
Aalborg University, Denmark

AALBORG UNIVERSITET
STUDENTERRAPPORT

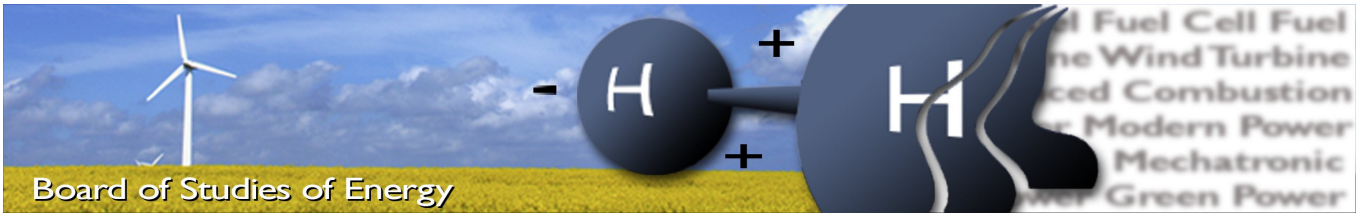

Title:	Control and Parameter identification of a Permanent Magnet Synchronous Motor with a L
Semester:	10th
Semester theme:	Master Thesis
Project period:	01.02.2013 to 04.06.2013
ECTS:	30
Supervisor:	Michael Mller Bech and Mehmet Sertug Basar
Project group:	1023

Anders Roland Pedersen

SYNOPSIS:

This report investigates the problems associated with having an inverter controlling a PMSM. Simulation models of the PMSM, the LC-filter and the inverter were created, as well was a controller the inverter currents, motor currents, motor voltages and the speed. However, due to time issues and incorrect measurements only a part of the controller was verified. It was, furthermore, investigated if the Recursive Least Squares method could be used to identify the parameters of the LC-filter, however, it was found that the approach used was lacking.

Copies:	4
Pages, total:	79
Appendix:	A-G
Supplements:	CD

By signing this document, each member of the group confirms that all participated in the project work and thereby all members are collectively liable for the content of the report.

Acknowledgement

I would like to thank my supervisors Michael Mller Bech and Mehmet Sertug Basar for their supervision and that they have spared their time to answer my questions.

I would like to thank my family and parents who have always been there for me and supported my, especially, I would like to thank my brother Harald who has helped me in many ways while I have been in Aalborg.

I would also like to give a thanks to Arne Mejlhede who has helped me through times of trouble kept me going.

Finally I would also like to thank the room mates, Venca Knap and Rakesh Sinha, at Aalborg University, for their company and friendship.

Contents

Chapter 1

Introduction

This chapter in contain the motivation of project, the problem statement and the problem limitation

1.1 Motivation

Due to the introduction of Voltage Source Inverters (VSI) in the early 1980s, it became possible to adjust the speed of AC motors and it quickly opened a lot of opportunities for the use of AC motors in industry. The ability to control the starting currents and the speed of the motor has brought the opportunity to also coordinate multiple motors so that complex processes have been made possible to handle. This precision control has, thus, brought an increase to the productivity of the industry in general.

In order to implement the control the AC motor a control strategy is also needed. For this Field Oriented Control (FOC) is the most popular control method applied. The FOC has the benefit of transforming the phase currents into two DC currents in the rotor reference frame. One controls the torque of the motor, while the other is related to the flux generated. This makes it possible to control the AC motor similar to the control of a DC motor.

The two major types of AC motors used in industry are the Induction Motor (IM) and the Permanent Magnet Synchronous Motor (PMSM). Compared to the IM, the PMSM has a higher energy efficiency. This is due to the fact that no extra energy is needed to magnetize the rotor, since it already contains permanent magnets. Due to the high efficiency a smaller rated PMSM can perform the same job as an IM with a higher rating.

The use of a VSI to drive an AC motor, however, also brings certain problems with it. The VSI introduces some negative effects in the AC motor. The common solution to solving these problems related with these negative effects is to place a LC-filter between the VSI and the motor. The LC-filter the attenuates the switching frequency from the inverter, and provides a more sinusoidal signal to the motor. The big problem with the unfilter VSI signal yield a high $\frac{du}{dt}$, which has some undesirable effects. The negative effects include:

- Increase in acoustical noise, generated by magnetical forces
- Wear of the bearings due to bearing currents
- Isolation stress of the stator windings in connection with long leads between the motor and the inverter

The acoustical noise generated can become an issue depending on where the motor is placed and what the specific national health regulations prescribe. The Danish regulations for noise with regards to industry prescribe a maximum noise level of 40-70 dB depending on how close the machinery is to a public residential area [1].

Undesired down time of the motor can be a huge financial loss for a company. The down time can be because of repair of the motor parts due to failures. As shown in Figure 1.1, [2], bearing failures and failures related to the stator windings are the two most predominant failure reasons with regards to large motors.

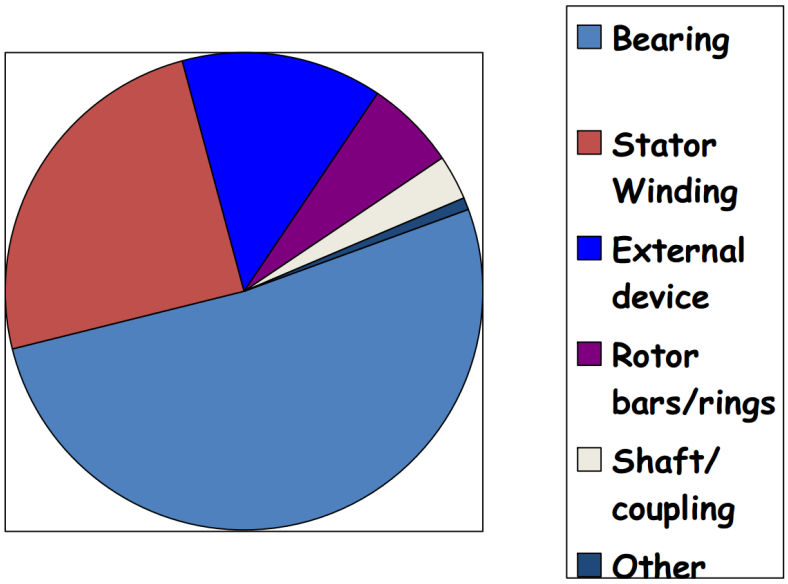

Figure 1.1: Pie chart of common motor failures for large motors, taken from [2]

The cost of failure may be even larger in case of the failure not being detected in time. The downtime costs may include things such as

- Repair or replacement of parts of the motor
- Replacing the entire the motor
- Man hours for labour
- Cost of related damaged industrial machinery
- Lost production

The failures may even result in accidents where people get injured or in worst case lose their lives.

The mentioned three negative effects introduced by the VSI, may all be solved by inserting a LC-filter between the VSI and the PMSM. The LC filter itself will, however, introduce some other problems. The LC-filter will change the characteristics of the voltages and currents measured at the motor terminals, due to the change in amplitude and phase introduced by the filter. For this reason it is necessary to construct a control strategy that accounts for the phase and amplitude changes.

Given a scenario where a customer buys a LC-filter, where the only information given is that it is made to attenuate switching frequencies higher than a specified frequency and work according to a specified bandwidth. Another scenario could be that the filter parameters seem to be inaccurate. In both of these scenarios it would be convenient if the filter parameter could be automatically identified by the VSI by simply connecting it, and letting the VSI run some estimate algorithms. So that the proper control can be set up.

By proper control is here meant a control strategy that accounts for the LC-filter and not just a regular FOC where certain condition have been set with regards to the maximum torque that can be produced.

1.2 Objective

The primary objective of this project is to create a controller that can control the PMSM with the a filter between it and the inverter, based on parameters for the system that are estimated. In order to achieve this goal the following things are investigated:

- How can the PMSM, VSI and filter modelled?
- How do the negative effects caused by the VSI occur in the PMSM?
- How is it possible to identify the parameters of filter?
- How is the PMSM controlled with a filter between the inverter and the motor?

1.3 Limitation

This report will focus on a LC-filter and a PMSM of type Surface Mounted with regards to the problem statement above.

The Recursive Least Squares method is a well known and has in many cases proven to yield good results, [4] and [3]. Furthermore the RLS method can be set up to take account for the presence of measurement noise. Based on this and the personal scientific curiosity it is chosen as the method for the parameter identification. It is for the identification assumed that the motor parameters already are known.

With regards to the control of the PMSM and the filter, the focus will be on finding a FOC-like method where all important states of the system are controlled. Here is referred to:

- The current out of the filter
- The current into the motor
- The voltage over the motor
- The speed of the motor

The control is required to control the speed of the motor by regulating the output voltages of the inverter.

1.4 Organisation of report

Firstly, in Chapter 2 the negative effects introduced by the VSI in the PMSM, are investigated. Here primarily three negative effects are considered: Bearing currents that damages the bearing; ringing overshoot voltages that are the effect of have long leads between the inverter and the PMSM; and the generation the magnetical vibrations that generate acoustical noise at the switching frequency and its harmonics. Different solutions to these problems are then considered of which the filter solution is one of them.

Then in Chapter 3, then the setup used is described, while Chapters 4-6 deal with modelling the PMSM, the VSI and the LC-filter, respectively.

In Chapter 7 the parameter identification of the LC-filter is attempted via use of the RLS-method. Here three different test configuration scenarios are investigated, and the test signal that excites all the needed frequencies is considered.

In Chapter 8 a control structure is proposed that controls the inverter currents, motor currents, motor voltages and the speed.

This controller is then tested on the setup in Chapter 9, and finally in Chapter 10 the conclusion is made.

Chapter 2

Negative effects introduced by the VSI in the PMSM

In this chapter, the negative effects of the VSI on the PMSM are firstly analysed and secondly possible solutions are suggested of which the LC-filter is one them. Specifically bearing currents and ringing overshoot at the motor terminal, which are an effect of long motor leads, will be investigated, as well as magnetic acoustical noise and other effects. Finally different solutions to these problems will be evaluated.

2.0.1 Bearing currents

There has within the recent decades been established a correlation between damaged bearings and the use of inverters for controlling motors. The damage of the bearings is in [5] meant to be caused partly by the existence of bearing currents. The existence of these bearing currents is in the following exemplified by looking at the inverter as a common mode voltage and current generator. Consider a single bridge DC to AC converter as illustrated in Figure 2.1.

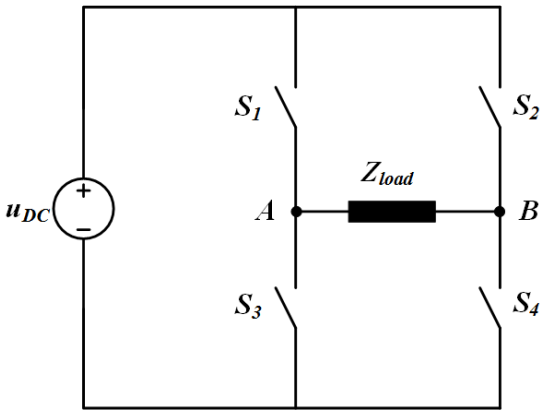

Figure 2.1: Single bridge converter with a load

Assume that the switches S_1 and S_2 are switched to the same state while S_3 and S_4 are switched to the opposite state. As there is no current that will flow through load impedance Z_{load}

because A and B will have the same voltage potential, the voltage potential at A or B relative to the point O would though have a periodic square-wave form, given a similar gating signal applied to the switches.

Assuming a parasitic capacitor exists somewhere between Z_{load} and ground, then current would flow through Z_{load} and the parasitic capacitor. The voltage potential at A and B relative to ground is called the common mode voltage, while the current through the parasitic capacitor is called the common mode current. This is illustrated in Figure 2.2.

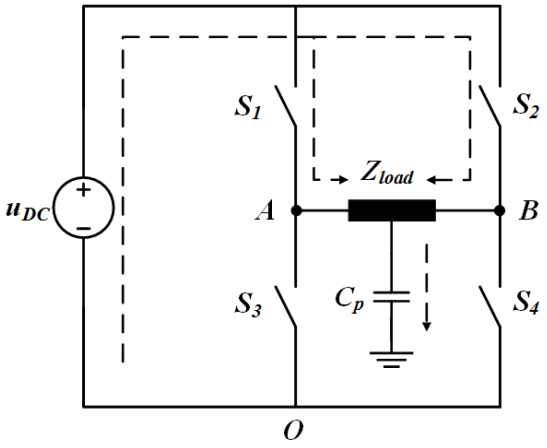

Figure 2.2: Single bridge converter with a load and a parasitic capacitor

In the case of the three phase inverter, the common mode voltages will be given by the voltage potential between the points A, B and C and the point O, denoted u_{AO}, u_{BO} and u_{CO} respectively. The points A, B, C and O are same as those found in Figure 5.1. In [5] it is shown that two parasitic coupling paths exist in an induction motor. In [6] it is stated that the same is also true for a PMSM. The parasitic coupling paths are illustrated in Figure 2.3.

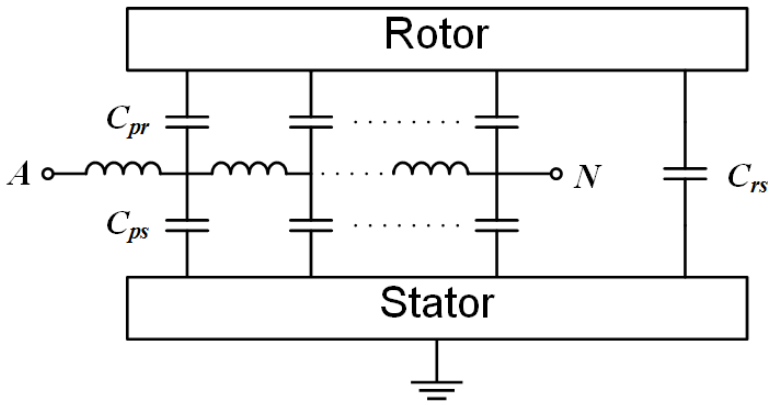

Figure 2.3: Parasitic couplings in the motor

One of the parasitic coupling paths is between the stator winding and the stator, where the parasitic capacitor is represented by C_{ps}. The other parasitic coupling path is between the stator windings and the rotor, where the parasitic capacitor is represented by C_{pr}. There also exists an airgap capacitance effect between the rotor and the stator, denoted C_{rs}, given that they are

electrically insulated.

As the bearing balls complexly rotate relative to each other and the bearing ball case, the bearing can be modelled as a switch that seemingly randomly changes its state. The circuit diagram for a single phase of this with the parasitic capacitances and the common mode voltage u_{AO} as input is shown in Figure 2.4.

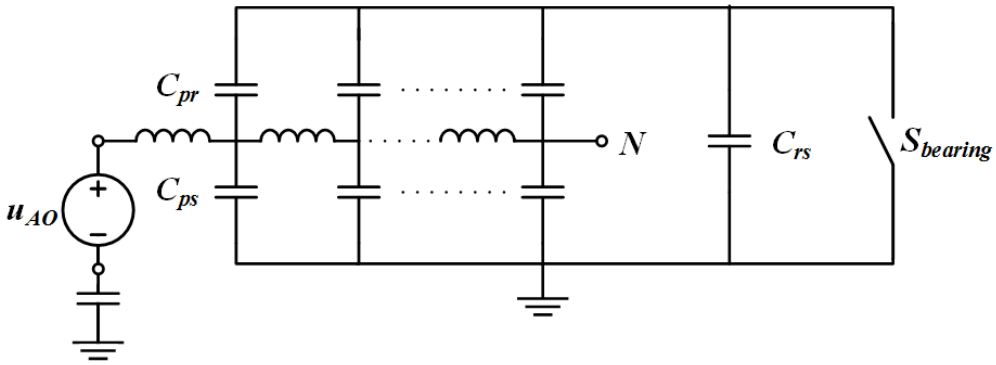

Figure 2.4: Parasitic couplings in the motor with the bearing as a random conduction switch

The impedance Z_{in} in the figure is the common mode internal impedance, which according to [5] mainly exists as parasitic coupling capacitance between O and the grounded inverter case.

The bearing current can be split into two types, conduction mode bearing current and discharge mode bearing current. The current that flows in the bearing continuously over a period of time due to good conductivity is called the conduction mode bearing current. In [5] it is further established that this type of current is related to the $\frac{du}{dt}$ of the PWM switching.

To illustrate the significance of how large $\frac{du}{dt}$ becomes as short example is made here. Given DC link voltage of 560 V, and switching time of $2\mu s$, the rate of voltage change is of the size $\frac{du}{dt} = 280 \cdot 10^6\ V/s$.

The discharge mode bearing current is as the name indicates, the current that is discharged via the airgap capacitor after a period of no conductivity. This spiky occurring current is, however, independent of as such, but due to its relation to the conductive mode bearing current. The size of the current spikes from the discharge mode bearing current can be related to the energy stored in the airgap capacitor, and thus to the switching sequence of the common mode voltages. In general the bearing currents depends on the switching frequency of the common mode voltages and the conductivity switching.

The discharge mode bearing current results in a microscopic melting of the bearing ball and the running track metal, which, over time, will mean the bearing may need to be replaced.

2.0.2 Effect of long motor leads

In the case of large machines, it can in industry often be found that the distance between the inverter and the motor is rather large, due to some practical reasons. The length of the cable in connection with the high $\frac{du}{dt}$ from the inverter output may, though, cause problems at the motor terminals resulting in voltage stresses in the stator winding insulations of the motor [7]. To understand this problem, it is necessary to look at the travelling wave voltage, u_c, and current, i_c, in the cable. u_c and i_c may be expressed in terms of the two wave equations (2.1) and (2.2) respectively.

$$\frac{1}{L_c C_c}\frac{d^2 u_c}{dx_c^2} = \frac{d^2 u_c}{dt^2} \tag{2.1}$$

$$\frac{d^2 i_c}{dx_c^2} = L_c C_c \frac{d^2 i_c}{dt^2} \tag{2.2}$$

x_c represents the distance traversed in the cable, and L_c and C_c are the leakage inductance and the cable coupling capacitance respectively. These wave equations are based on a non-resistance single phase two-wire cable as illustrated in Figure 2.5.

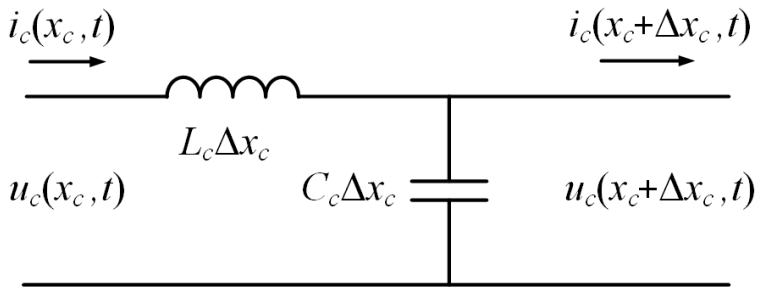

Figure 2.5: Single phase cable with the length Δx_c

The solutions to (2.1) and (2.2) are given as (2.3) and (2.4) respectively, [7].

$$u_c(x,t) = u_c^+(t - \sqrt{L_c C_c}x_c) + u_c^-(t + \sqrt{L_c C_c}x_c) \tag{2.3}$$

$$i_c(x,t) = i_c^+(t - \sqrt{L_c C_c}x_c) + i_c^-(t + \sqrt{L_c C_c}x_c) \tag{2.4}$$

The negative and positive superscripts in the solution indicate which way the waves are travelling in the cable. In other words, this deduces that there are waves that travel in the opposite direction than from inverter to motor. The cause of these waves is due to voltage reflection, happening at the end of the cable, or in the case of the connected PMSM at the terminal of the stator windings. The size of the reflected wave is defined by the input wave in reverse order and multiplied by a reflection coefficient. The voltage reflection coefficient at the load and the voltage source may be expressed as (2.5) and (2.5) respectively, [7].

$$\Gamma_l = \frac{R_l - R_c}{R_l + R_c} \tag{2.5}$$

$$\Gamma_s = \frac{R_s - R_c}{R_s + R_c} \tag{2.6}$$

where R_l and R_s are the load and source resistance respectively, while R_c is the characteristic resistance which is expressed as

$$R_c = \sqrt{\frac{L_c}{C_c}} \tag{2.7}$$

This wave reflection leads to a ringing voltage overshoot at the motor terminals as seen in Figure 2.6. According to [8] where the figure is taken from, parallel cables result in a reduced characteristic impedance, which yields a higher reflection coefficient and hence a larger overshoot.

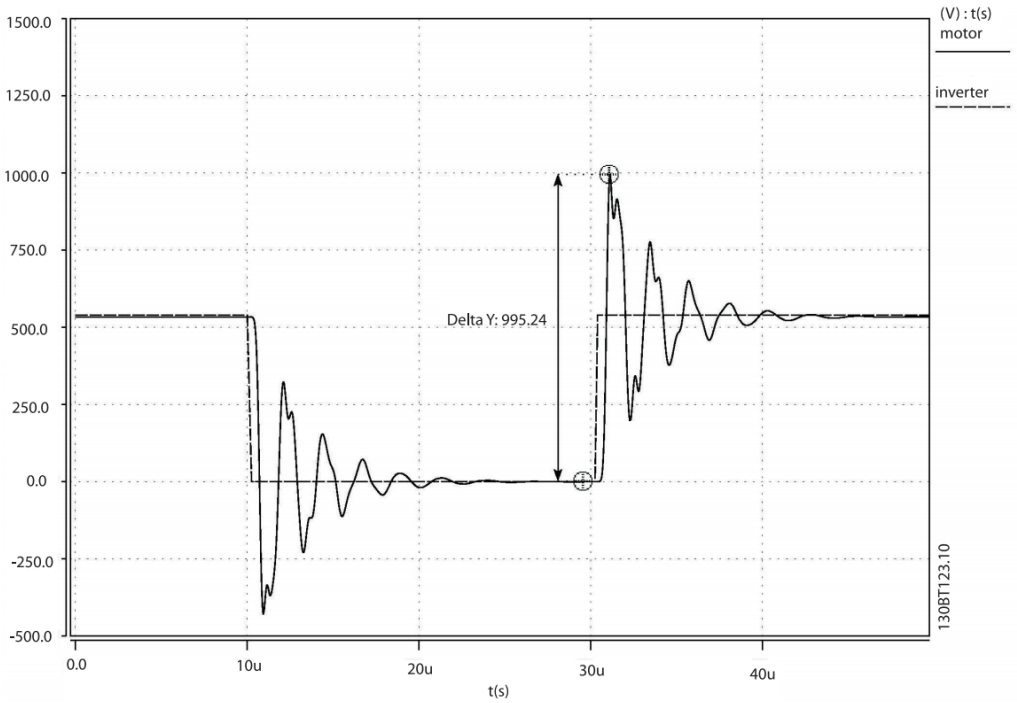

Figure 2.6: Ringing voltage overshoot at motor terminal, taken from [8]

According to [9] the combination of low rising times and long cable may have hazardous effect on the insulation of the motor, due to the large overshoot as illustrated. The stresses in the insulation will over time result in a need to repair or replace the motor.

2.0.3 Acoustical noise generated by magnetical forces

The electromagnetical torque of the PMSM is essentially produced by tangential forces generated in the stator windings which make the rotor rotate. According to [10] these tangential forces will cause unwanted tangential vibrations in the stator frame. This, thus, means the stator

frame will effectively vibrate at the switching frequency of the inverter and its harmonics. These vibration will create acoustical noise, which as mentioned can be highly undesirable depending on the application and the location. Damaged bearings, caused by bearing current, can also be a contributing fact to the acoustical noise generated.

2.0.4 Other effects caused by the use of a VSI to drive a PMSM

The voltage ringing at the terminals is not the only type of noise present in the cables. The common mode voltage as already discussed also contribute to noise in the cables.

In [11] it is found that under Maximum Torque Control, the iron losses are primarily caused by the carrier of the PWM inverter. This means that effectively more power is needed to drive the motor.

2.1 Solutions

With regards to the bearing currents, there are two solutions. One is to suppress these currents the other is to circumvent them. Suppressing them can simply be done by inserting a filter between the inverter and the motor, which would attenuate the high switching frequency and thus reduce the common mode voltages and in turn the bearing currents themselves. The circumvention of the bearing currents could be made placing a brush from rotor to stator and thus deviate the current. Another method could be to use conductive bearing lubrication.

One open ended solution to ringing voltage overshoot problem could be to reduce the reflection coefficient at the motor terminal in some way, this essentially done by reducing the load resistance, R_l. How this could be done specifically is not addressed in this project. A second solution could be to filter the signal and thereby reduce the ringing voltage overshoot.

The filter option is also a solution to the acoustical noise problem caused by the VSI as well as for electromagnetical noise in the cable produced by the common mode voltages. The electromagnetical noise in the cable can also be reduced practically by using shielded cables and approriate layouting with regards to electromagnetical producing sources. Placing the cables in grounded cable tray might also be advisable.

Finally the filter can also be used to reduce the iron losses introduced by the VSI as mentioned. The energy loss, due to the introduction of the filter itself may though not justice the merit, of using the filter, compared to the energy saved by reducing the iron losses. These calculations are not within the scope of this project. However, given that the filter solution also solves some of the other problem, the decrease in iron losses is just an added benefit to this solution.

Based on the above the filtering option is a general good, valid and justifiable solution to solving the negative effects introduced by the VSI that are discussed here.

Chapter 3

Test Setup

This chapter describes the test setup used for verifying the parameter identification and the controller. The test setup utilized is a dSPACE setup,[12].

3.1 dSPACE setup

The controller is implemented in MATLAB's Simulink and compiled and then downloaded into a dSPACE DS1103 PPC, by utilizing a special dSPACE toolkit in Simulink. The program is then executed in the dSPACE DS1103 PPC. The dSPACE DS1103 PPC is a powerful floating point mixed RISC/DSP controller that has I/O connections. These input connections are used for reading the measurement signals received from the position sensor and the LEM modules used for measuring the currents and voltages. While the output signal is transmitted to the inverter.

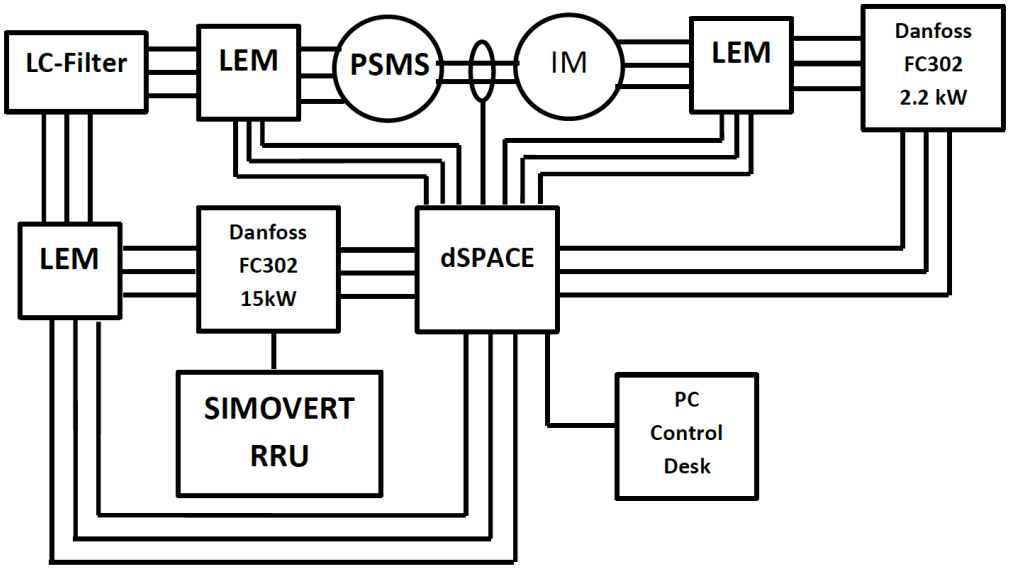

Figure 3.1: Diagram of the dSPACE setup

As shown in Figure 3.1, which show a diagram of the physical setup used, the setup consists of

two inverters and a PMSM and an IM that are connected via their shafts, as well as the LC-filter between one of the inverters and the PMSM. The PMSM is a Siemens ROTEC 1FT6084-8SH7 while the IM is a ABB M2AA100LA. The specification for the PMSM can be found in Appendix D. The two inverters are Danfoss FC302 with an attached IPC2 (Interface and Protection Card) that makes it possible to control the IGBT drivers from the dSPACE DS1103 PPC, while providing reliable short-circuit, short-through, DC-overvoltage and over-temperature protections, [12]. The deadtime of the switches can be set to the values: $2.0\mu s$, $2.5\mu s$, $3.0\mu s$ and $4.0\mu s$. The system is set up to run with a sampling frequency of 5 kHz. The PMSM is driven by a 15 kW version of the Danfoss FC302, while the IM is driven by a 2.2 kW version. The DC-link of the inverter for the PMSM is provided by a Siemens SIMOVERT RRU regenerative rectifier of type 6SE7028-6EC85-1AA0, which is set to provide 560 V. In Figure 3.2 is shown a photo of the setup with text indicating where the different parts are.

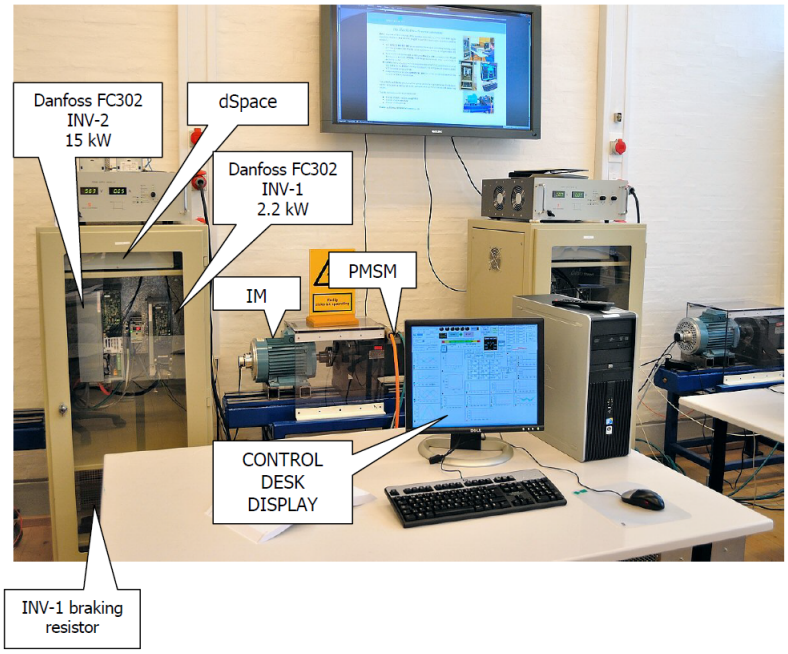

Figure 3.2: Photo of the dSPACE setup, taken from [12]

The PMSM and IM can be controlled in real-time from a PC via a software called Control Desk. For this there already exist a control environment that enable control of the IM and PMSM without filter in torque and speed mode. Control Desk also provides the oppotunity of displaying the measured signals in more or less real-time, and saving these. In Figure 3.3 is shown that provide user interface.

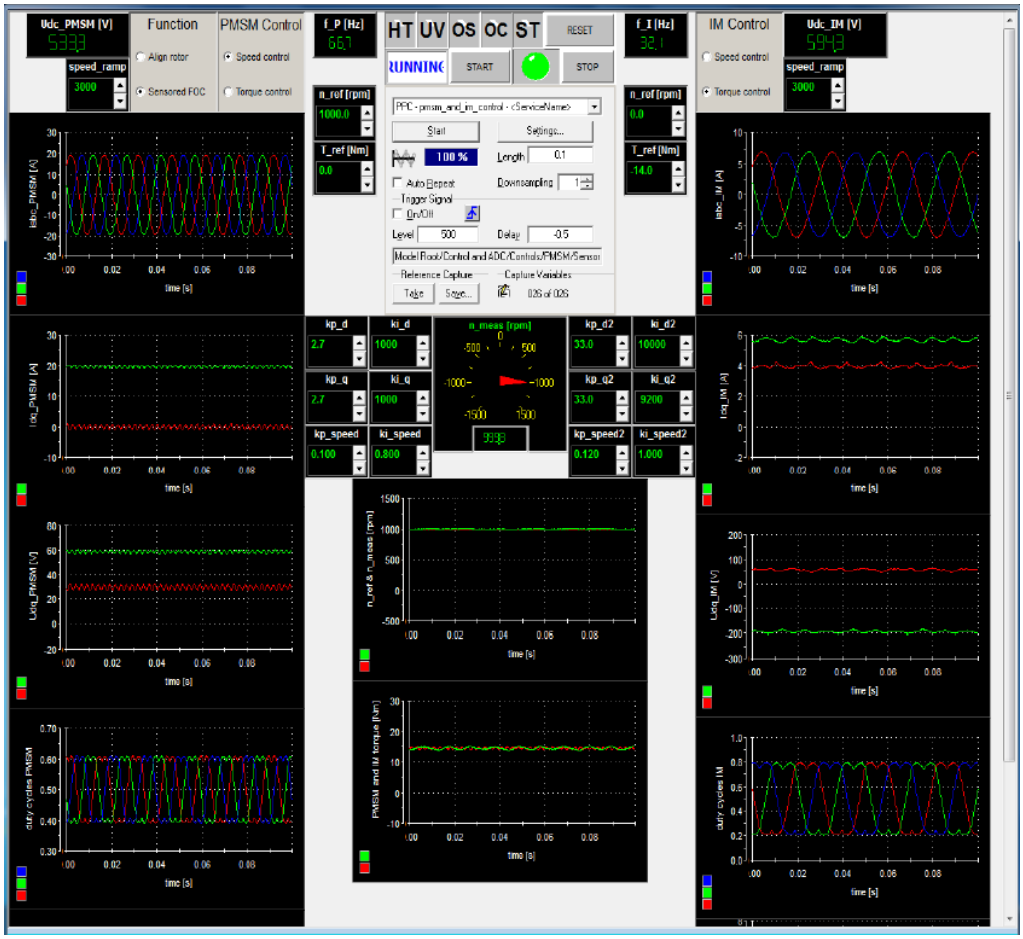

Figure 3.3: Screenshot of the Control Desk UI

Chapter 4

Model of a PMSM

This chapter contains the modelling of the PMSM, which is split up into three parts: Modelling of the electrical part of the PMSM, modelling of the electromagnetical torque and finally the modelling the mechanical system, [18] and [19]

4.1 Modelling of the Electrical System of the PMSM

The electrical part of the PMSM can in principle be modelled as three sets of resistances and inductances connected in a Y-connection as illustrated in Figure 4.1.

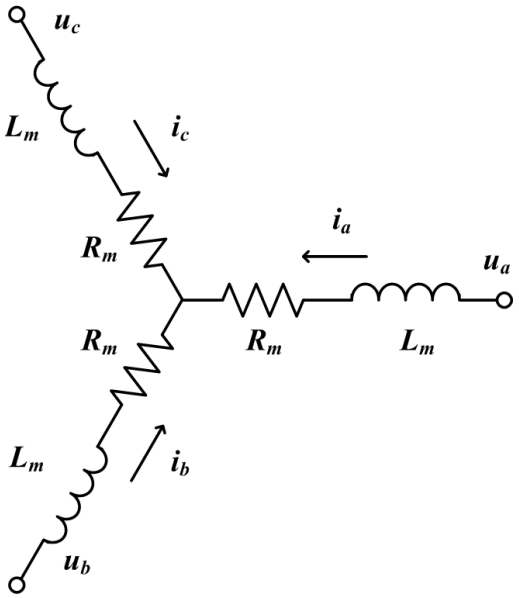

Figure 4.1: Schematic of the PMSM representation

Which can thus be described by the following set of differential equations

$$\begin{bmatrix} u_{ma} \\ u_{mb} \\ u_{mc} \end{bmatrix} = \begin{bmatrix} R_m & 0 & 0 \\ 0 & R_m & 0 \\ 0 & 0 & R_m \end{bmatrix} \begin{bmatrix} i_{ma} \\ i_{mb} \\ i_{mc} \end{bmatrix} + \frac{d}{dt} \begin{bmatrix} \lambda_{ma} \\ \lambda_{mb} \\ \lambda_{mc} \end{bmatrix} \Leftrightarrow \tag{4.1}$$

$$\mathbf{u_{mabc}} = \mathbf{R_m i_{mabc}} + \frac{d}{dt}\boldsymbol{\lambda}_{\mathbf{mabc}} \tag{4.2}$$

Where u and i are the voltages applied to a phase and its measured currents, λ is the flux linkage of the windings. The subscribts ma,mb and mc represents their association to the three phases. Lastly R_m is the resistance of the phase windings. As the flux linkages, $\lambda_m a$, $\lambda_m b$ and $\lambda_m c$, of the stator change so they will drive the angular position, θ_e, of the permanent magnet rotor to also change, and vice versa. As the permanent magnet rotates, its the flux linkage will also affect $\lambda_m a$, $\lambda_m b$ and $\lambda_m c$. The flux linkage vector of the stator can be found through the relationship of (4.3)

$$\boldsymbol{\lambda}_{\mathbf{mabc}} = \mathbf{L_{mabc}}(\theta_e) \cdot \mathbf{i_{mabc}} + \boldsymbol{\lambda}_{\mathbf{abcpm}}(\theta_e) \tag{4.3}$$

where $\mathbf{L_{mabc}}(\theta_e)$ is an inductance matrix containing the mutual, self and leakage inductances of the stator windings where all of which depend on θ_e, the derivation of the inductance matrix may be found in Appendix A. The mutual flux between the stator and the rotor is represented by equation 4.4

$$\boldsymbol{\lambda}_{\mathbf{abcpm}}(\theta_e) = \lambda_{pm} \begin{bmatrix} \cos(\theta_e) \\ \cos\left(\theta_e - \frac{2\pi}{3}\right) \\ \cos\left(\theta_e + \frac{2\pi}{3}\right) \end{bmatrix} \tag{4.4}$$

For the purpose of simplifying the model, a Clark transformation that reduces the three phases to the two main components α and β, and a Park transformation that removes their dependency of θ_e, are applied to the voltage equation of the PMSM. The total transformation matrix from abc to dq and the inverse from dq to abc are given by (4.5) and (4.6) respectively. In Figure 4.2 is shown the geometrical relations between $\alpha\beta$ and dq, The α-axis coincides with the a-axis shown in Figure 4.1.

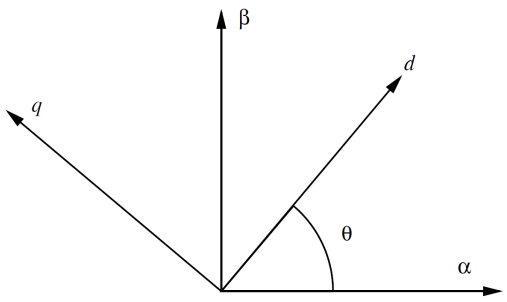

Figure 4.2: the geometrical relations between $\alpha\beta$ and dq

$$\mathbf{T} = \frac{2}{3}\begin{bmatrix} \cos(\theta_e) & \cos\left(\theta_e - \frac{2\pi}{3}\right) & \cos\left(\theta_e + \frac{2\pi}{3}\right) \\ \sin(\theta_e) & \sin\left(\theta_e - \frac{2\pi}{3}\right) & \sin\left(\theta_e + \frac{2\pi}{3}\right) \\ \frac{1}{2} & \frac{1}{2} & \frac{1}{2} \end{bmatrix} \tag{4.5}$$

$$\mathbf{T}^{-1} = \begin{bmatrix} \cos(\theta_e) & \sin(\theta_e) & 1 \\ \cos\left(\theta_e - \frac{2\pi}{3}\right) & \sin\left(\theta_e - \frac{2\pi}{3}\right) & 1 \\ \cos\left(\theta_e + \frac{2\pi}{3}\right) & \sin\left(\theta_e + \frac{2\pi}{3}\right) & 1 \end{bmatrix} \tag{4.6}$$

Applying the transformation to $\mathbf{u_{mabc}}$, $\mathbf{u_{mabc}}$ and $\boldsymbol{\lambda}_{\mathbf{mabc}}$,(4.2) can be rewritten to its dq-equivalent as shown in the following derivation.

$$\left(\mathbf{T}^{-1}\mathbf{u_{mdq0}}\right) = \mathbf{R_m}\left(\mathbf{T}^{-1}\mathbf{i_{mdq0}}\right) + \tfrac{d}{dt}\left(\mathbf{T}^{-1}\boldsymbol{\lambda}_{\mathbf{mdq0}}\right) \Leftrightarrow \tag{4.7}$$

$$\mathbf{T}\left(\mathbf{T}^{-1}\mathbf{u_{mdq0}}\right) = \mathbf{T}\mathbf{R_m}\left(\mathbf{T}^{-1}\mathbf{i_{mdq0}}\right) + \mathbf{T}\tfrac{d}{dt}\left(\mathbf{T}^{-1}\boldsymbol{\lambda}_{\mathbf{mdq0}}\right) \Leftrightarrow \tag{4.8}$$

$$\mathbf{u_{mdq0}} = \mathbf{R_m}\mathbf{i_{mdq0}} + \mathbf{T}\left(\left(\tfrac{d}{dt}\mathbf{T}^{-1}\right)\boldsymbol{\lambda}_{\mathbf{mdq0}} + \mathbf{T}^{-1}\left(\tfrac{d}{dt}\boldsymbol{\lambda}_{\mathbf{mdq0}}\right)\right) \Leftrightarrow \tag{4.9}$$

$$\mathbf{u_{mdq0}} = \mathbf{R_m}\mathbf{i_{mdq0}} + \mathbf{T}\left(\tfrac{d}{dt}\mathbf{T}^{-1}\right)\boldsymbol{\lambda}_{\mathbf{mdq0}} + \tfrac{d}{dt}\boldsymbol{\lambda}_{\mathbf{mdq0}} \Leftrightarrow \tag{4.10}$$

$$\mathbf{u_{mdq0}} = \mathbf{R_m}\mathbf{i_{mdq0}} + \omega_e\mathbf{J_T}\boldsymbol{\lambda}_{\mathbf{mdq0}} + \tfrac{d}{dt}\boldsymbol{\lambda}_{\mathbf{mdq0}} \tag{4.11}$$

$$\mathbf{T}\left(\tfrac{d}{dt}\mathbf{T}^{-1}\right) = \omega_e\begin{bmatrix} 0 & -1 & 0 \\ 1 & 0 & 0 \\ 0 & 0 & 0 \end{bmatrix} = \omega_e\mathbf{J_T} \tag{4.12}$$

In a similar fashion the flux linkage of (4.3) is transformed below

$$\mathbf{T}^{-1}\boldsymbol{\lambda}_{\mathbf{mdq0}} = \mathbf{L_{mabc}}(\theta_e)\cdot\mathbf{T}^{-1}\mathbf{i_{mdq0}} + \boldsymbol{\lambda}_{\mathbf{abcpm}}(\theta_e) \Leftrightarrow \tag{4.13}$$

$$\mathbf{T}\mathbf{T}^{-1}\boldsymbol{\lambda}_{\mathbf{mdq0}} = \mathbf{T}\mathbf{L_{mabc}}(\theta_e)\cdot\mathbf{T}^{-1}\mathbf{i_{mdq0}} + \mathbf{T}\boldsymbol{\lambda}_{\mathbf{abcpm}}(\theta_e) \Leftrightarrow \tag{4.14}$$

$$\boldsymbol{\lambda}_{\mathbf{mdq0}} = \mathbf{L_{mdq0}}\mathbf{i_{mdq0}} + \boldsymbol{\lambda}_{\mathbf{dq0pm}} \tag{4.15}$$

$$\mathbf{L_{mdq0}} = \begin{bmatrix} L_{md}^* + L_{ls} & 0 & 0 \\ 0 & L_{mq}^* + L_{ls} & 0 \\ 0 & 0 & L_{ls} \end{bmatrix} = \begin{bmatrix} L_{md} & 0 & 0 \\ 0 & L_{mq} & 0 \\ 0 & 0 & L_{ls} \end{bmatrix} \tag{4.16}$$

$$\boldsymbol{\lambda}_{\mathbf{dq0pm}} = \begin{bmatrix} \lambda_{pm} \\ 0 \\ 0 \end{bmatrix} \tag{4.17}$$

Inserting (4.15) into (4.11) the d- and q-axis voltage equations for the surface mounted PMSM ($L_m = L_d = L_q$) can be written as

$$u_{md} = R_m i_{md} - \omega_e L_m i_{mq} + L_m \frac{di_{md}}{dt} \tag{4.18}$$

$$u_{mq} = R_m i_{mq} + \omega_e L_m i_{md} + L_m \frac{di_{mq}}{dt} + \omega_e \lambda_{pm} \tag{4.19}$$

$$\tag{4.20}$$

4.2 Modelling of the Electromagnetical Torque

The Electromagnetical torque produced by the PMSM can be found through its relationship to the mechanical power produced by the PMSM

$$\tau_e = \frac{P_m}{\omega_m} \tag{4.21}$$

The electrical instantaneous power dq0-space is given by

$$\begin{aligned} P_{inmdq0} &= \mathbf{i_{mdq0}}^T \mathbf{u_{mdq0}} \\ &= \mathbf{R_m} \mathbf{i_{mdq0}}^T \mathbf{i_{mdq0}} + \mathbf{i_{mdq0}}^T \frac{d}{dt} \boldsymbol{\lambda}_{\mathbf{mdq0}} + \omega_e \mathbf{i_{mdq0}}^T \mathbf{J_T} \boldsymbol{\lambda}_{\mathbf{mdq0}} \end{aligned} \tag{4.22}$$

The relationship between the electrical instantaneous power in the abc-space and its dq0-space equivalent is given by (4.23).

$$\begin{aligned} P_{inmabc} &= \mathbf{i_{mabc}}^T \mathbf{u_{mabc}} = \mathbf{i_{mabc}}^T \mathbf{T}^{-1} \mathbf{T} \mathbf{u_{mabc}} = \mathbf{i_{mabc}}^T \mathbf{T}^{-1} \mathbf{u_{mdq0}} \\ &= \left(\mathbf{T}^{-1} \mathbf{T} \mathbf{i_{mabc}}\right)^T \mathbf{T}^{-1} \mathbf{u_{mdq0}} = \left(\mathbf{T}^{-1} \mathbf{i_{mdq0}}\right)^T \mathbf{T}^{-1} \mathbf{u_{mdq0}} \\ &= \mathbf{i_{mdq0}}^T \left(\mathbf{T}^{-1}\right)^T \mathbf{T}^{-1} \mathbf{u_{mdq0}} = \frac{3}{2} \mathbf{i_{mdq0}}^T \mathbf{u_{mdq0}} \end{aligned} \tag{4.23}$$

Combining (4.22) and (4.23) the electrical instantaneous power in the abc-space can thus be described in terms of d and q components of the voltages and currents.

$$\begin{aligned} P_{inmabc} &= \frac{3}{2} \mathbf{i_{mdq0}}^T \mathbf{u_{mdq0}} \\ &= \frac{3}{2} \mathbf{R_m} \mathbf{i_{mdq0}}^T \mathbf{i_{mdq0}} + \frac{3}{2} \mathbf{i_{mdq0}}^T \frac{d}{dt} \boldsymbol{\lambda}_{\mathbf{mdq0}} + \frac{3}{2} \omega_e \mathbf{i_{mdq0}}^T \mathbf{J_T} \boldsymbol{\lambda}_{\mathbf{mdq0}} \end{aligned} \tag{4.24}$$

The three power terms in (4.24) are respectively the copper loss, the change of the energy stored in the magnetic field, and finally the mechanical output power, P_m. The electromagnetical torque is thus given as

$$\tau_e = \frac{3}{2} \frac{\omega_e}{\omega_m} \mathbf{i_{mdq0}}^T \mathbf{J_T} \boldsymbol{\lambda}_{\mathbf{mdq0}} \tag{4.25}$$

using that $\omega_e = N_{pp}\omega_m$ and inserting (4.15), τ_e can be rewritten to

$$\tau_e = \quad \tfrac{3}{2} N_{pp} \mathbf{i_{mdq0}}^T \mathbf{J_T} \left(\mathbf{L_{mdq0}} \mathbf{i_{mdq0}} + \boldsymbol{\lambda}_{\mathbf{dq0pm}} \right) \quad = \frac{3}{2} N_{pp} \left(\lambda_{pm} i_q + (L_d - L_q) i_d i_q \right) \tag{4.26}$$

For the surface mounted PMSM, where $L_d = L_q$, the electromagnetical torque equation can be further reduced to

$$\tau_e = \frac{3}{2} N_{pp} \lambda_{pm} i_q \tag{4.27}$$

Writting the currents in polar form as in (4.28) and (4.29)

$$i_d = |\mathbf{i_{mdq}}| \cos \rho \tag{4.28}$$

$$i_q = |\mathbf{i_{mdq}}| \sin \rho \tag{4.29}$$

where ρ is the angle between the space vector of the motor current, $\mathbf{i_{mdq}}$, and the d-axis, and ρ is called the torque angle. The torque then be written as

$$\tau_e = \frac{3}{2} N_{pp} \lambda_{pm} |\mathbf{i_{mdq}}| \sin \rho \tag{4.30}$$

4.3 Modelling of the Mechanical System

Using Newton's second law the torque equation of the motor can be written as

$$J \frac{d\omega_m}{dt} = \tau_e - B_{fric} \omega_m \tag{4.31}$$

It is from past experience of working with the same setup known that the friction coefficient of the system is significantly small enough to be ignored. The other parameters of the system can be found in the table in Appendix D.

The torque equation for the motor can thus be written as

$$\frac{J}{N_{pp}} \frac{d\omega_e}{dt} = \tau_e \Leftrightarrow \tag{4.32}$$

$$\frac{d\omega_e}{dt} = \frac{3}{2J} N_{pp}^2 \lambda_{pm} i_q \tag{4.33}$$

Chapter 5

Voltage Source Inverter

In this chapter the Voltage Source Inverter is modelled, [20], [21] and [22]

5.1 VSI

The PMSM is driven by a Voltage Source Inverter (VSI) which is controlled by the Space Vector Modulation (SVM) scheme. The goal of the VSI is to provide the AC voltages for the PMSM. This is done by converting a DC link voltage to a PWM signal. For this, three sets of switches are utilized as shown in Figure 5.1.

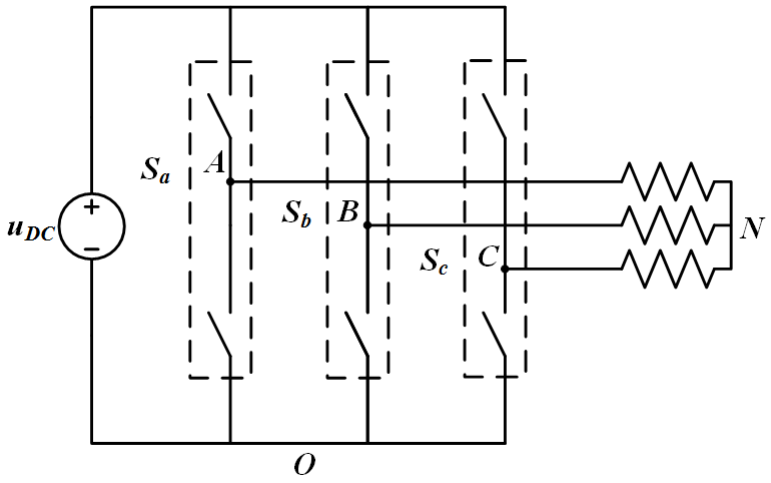

Figure 5.1: Voltage source inverter diagram

The two switches in each leg, can be relayed to either provide a state S of 1 representing ON or a state of 0 representing OFF for the applied load. The top and bottom switches should be in different states so as to not create a short circuit. Furthermore, freewheeling diodes should also be placed over each of the switches to prevent alternate current paths through some of the other switches. The output line-to-line voltages of the VSI may be expressed by the switch states of each leg as seen in (5.1).

$$\begin{bmatrix} u_{AB} \\ u_{BC} \\ u_{CA} \end{bmatrix} = u_{dc} \begin{bmatrix} 1 & -1 & 0 \\ 0 & 1 & -1 \\ -1 & 0 & 1 \end{bmatrix} \begin{bmatrix} S_a \\ S_b \\ S_c \end{bmatrix} \tag{5.1}$$

Given that the inverter is applied to a balanced Y-connected load, the following relationship holds true

$$u_{AN} + u_{BN} + u_{CN} = 0 \tag{5.2}$$

Furthermore, (5.3)-(5.5) below also hold true

$$u_{AB} = u_{AN} - u_{BN} \tag{5.3}$$
$$u_{BC} = u_{BN} - u_{CN} \tag{5.4}$$
$$u_{CA} = u_{CN} - u_{AN} \tag{5.5}$$
$$\tag{5.6}$$

Utilizing (5.2)-(5.5) the following relation between the line-to-line and the line-to-neutral voltages can be set up as

$$\begin{bmatrix} u_{AN} \\ u_{BN} \\ u_{CN} \end{bmatrix} = \frac{1}{3} \begin{bmatrix} 1 & 0 & -1 \\ -1 & 1 & 0 \\ 0 & -1 & 1 \end{bmatrix} \begin{bmatrix} u_{AB} \\ u_{BC} \\ u_{CA} \end{bmatrix} \tag{5.7}$$

Combining (5.1)-(5.7) the relation between the switch states and the line-to-neutral voltages can be expressed as

$$\begin{bmatrix} u_{AN} \\ u_{BN} \\ u_{CN} \end{bmatrix} = \frac{u_{dc}}{3} \begin{bmatrix} 2 & -1 & -1 \\ -1 & 2 & -1 \\ -1 & -1 & 2 \end{bmatrix} \begin{bmatrix} S_a \\ S_b \\ S_c \end{bmatrix} \tag{5.8}$$

The switching states may be set according to various modulation strategies that have the purpose of creating a sine like wave pattern that makes the motor rotate. Space Vector Pulse Width Modulation (SVPWM) is a popular choice for modulation. The details of SVPWM may be found in Appendix B.

Chapter 6

LC-filter

In this chapter the model of the LC is derived for a single phase firstly, and secondly the equations for the dq-transformed three phase LC-filter are provided [16], lastly simulations of the inverter voltages compare with the motor voltages are shown.

6.1 Model of the LC-filter

The large $\frac{du}{dt}$ problem associated with the use of a VSI to drive the PMSM may be diminished by introducing a LC-filter between the VSI and the PMSM. However, introducing a LC-filter will also change the gain and phase of the voltage signals feeding the PMSM, it is, therefore, important to model and analyse the behaviour of the LC-filter. In Figure 6.1 is shown the circuit diagram of a LC-filter for a single phase.

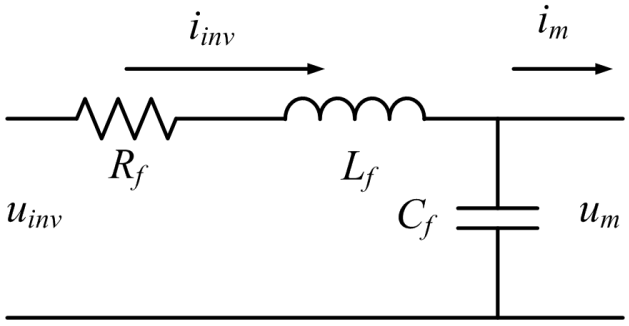

Figure 6.1: Circuit diagram of the LC-filter

Using Kirchhoff's voltage and current law, the following differential equations can be set up

$$u_{inv} = R_f i_{inv} + L_f \frac{di_{inv}}{dt} + u_m \tag{6.1}$$

$$i_{inv} = C_f \frac{du_m}{dt} + i_m \tag{6.2}$$

Taking the Laplace and using the principal of voltage division the transfer function of the LC-filter can be found.

$$\begin{aligned}\frac{u_m}{u_{inv}} &= \frac{Z_{RLC2}}{Z_{RLC1}+Z_{RLC2}} = \frac{1}{L_f C_f s^2 + C_f R_f s + 1} \\ &= \frac{\omega_{nRLC}^2}{s^2 + 2\zeta_{RLC}\omega_{nRLC}s + \omega_{nRLC}^2} \\ Z_{RLC1} &= R_f + L_f s \quad , \quad Z_{RLC2} = \frac{1}{Cfs}\end{aligned} \tag{6.3}$$

where ω_{nRLC} and ζ_{RLC} is natural frequency and the dampening of the filter respectively. Z_{RLC2} represents the impedance of the capacitor, and Z_{RLC1} represent the filter resistance combined with the filter inductance. In Figure 6.2 is shown the bode plot of the transfer function from equation (6.3), using the parameter from table in Appendix D.

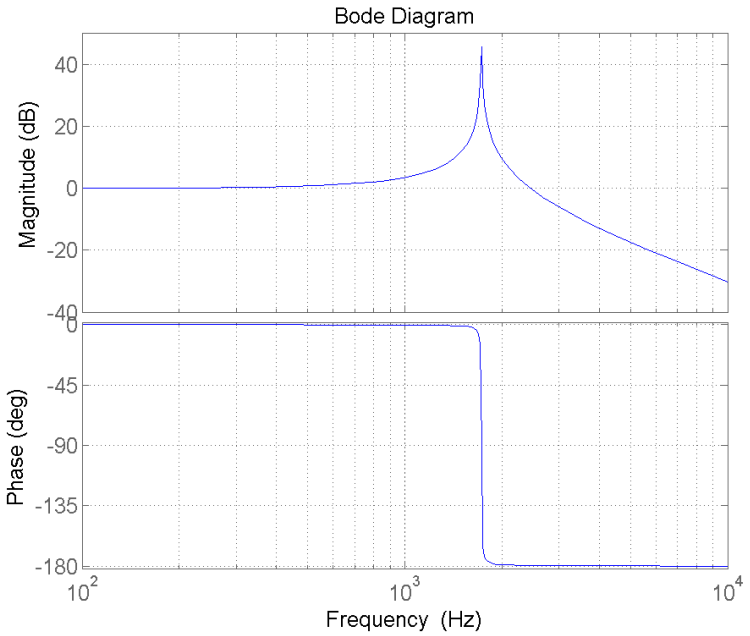

Figure 6.2: Bode plot of the LC-filter

For an under-dampened second order as is the case here, the resonance peak may be found at the natural frequency which for the LC-filter is given by

$$\omega_{nRLC} = \sqrt{\frac{1}{L_f C_f}} \tag{6.4}$$

Due to the amplification in the frequency range near the resonance peak, it is desirable to place this resonance peak in between the bandwidth of the PMSM and the switching frequency of the VSI. As to not amplify the control signal for the PMSM while attenuating the switching frequency.

For model convenience and later control, the three phase LC-filter is as with the PMSM model also transformed to its dq-equivalent, yielding equations (6.5)-(6.8). The derivation is the same as for the PMSM transform, and may be found in Appendix C.

$$u_{invd} = R_f i_{invd} - \omega_e L_f i_{invq} + L_f \frac{di_{invd}}{dt} + u_{md} \tag{6.5}$$

$$u_{invq} = R_f i_{invq} + \omega_e L_f i_{invd} + L_f \frac{di_{invq}}{dt} + u_{mq} \tag{6.6}$$

$$i_{invd} = -\omega_e C_f u_{mq} + C_f \frac{du_{md}}{dt} + i_{md} \tag{6.7}$$

$$i_{invq} = \omega_e C_f u_{md} + C_f \frac{du_{mq}}{dt} + i_{mq} \tag{6.8}$$

In Figure 6.3 is showm simulated results, where u_{inv} is compared with u_m, and can be observed the filter attenuates the switching frequency of the inverter

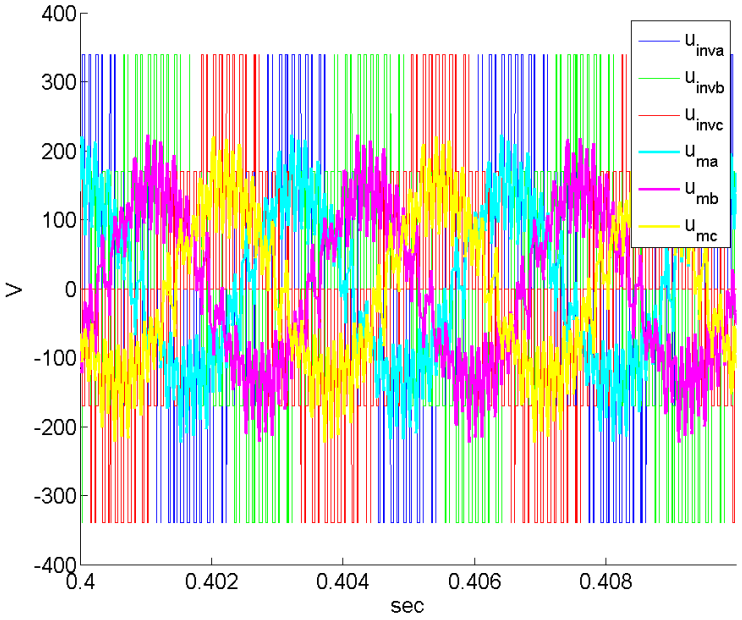

Figure 6.3: u_{inv} is compared with u_m

In Figure 6.4 is shown the inverter voltage reference signal, u_{invref}, compared with u_m.

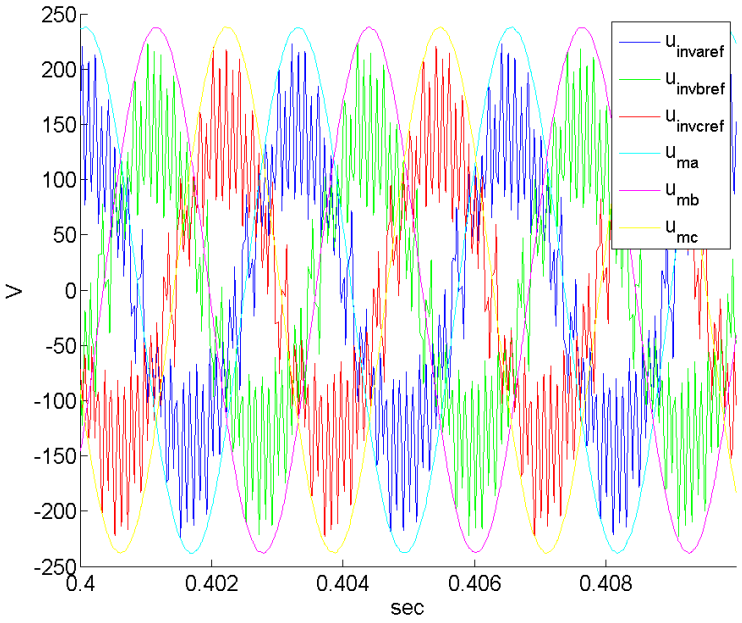

Figure 6.4: u_{invref} compared with u_m

Chapter 7

Parameter identification of the LC-filter

This chapter will investigate three possible test configurations for identifying the parameters of the LC-filter. For the indepentification the Least Squares (LS) method and the Recursive Least Squares (RLS) method are used, both of which also are described here.

7.1 The LS method and RLS method

The parameters of the LC-filter in each configuration will, first, be attempted to be found using the LS method under ideal conditions, meaning no noise is added to the simulations. The LS method attempts to fit the measured output with the estimated output of a model called the linear regression model. The linear regression model in (7.1) describes the output at a certain time as the multiplication of the vectors $\boldsymbol{\phi}(t)$ and $\boldsymbol{\theta_p}$.

$$y = \boldsymbol{\phi}^T \boldsymbol{\theta_p} \tag{7.1}$$

where $\boldsymbol{\phi}$ is called the linear regression vector, and contains information of previous input and output and the current input, depending on the model it represents. $\boldsymbol{\theta_p}$ is called the parameter vector, and contains the parameters that are sought to be estimated. The LS method is given by (7.2). The derivation may be found in Appendix D, [13].

$$\hat{\boldsymbol{\theta}}_p = \left[\sum_{i=1}^{t} \boldsymbol{\phi}(i)\boldsymbol{\phi}(i)^T\right]^{-1} \sum_{i=1}^{t} \boldsymbol{\phi}(i)y(i) \tag{7.2}$$

If the ideal condition check is passed, noise is added to the simulation, and the parameters are attempted to be found using the Recursive Least Squares (RLS) method. The RLS method can be set up to take the presence of noise into account, as for each sample, it updates its linear least squares estimate. This form of the RLS is called the Joseph form and is given by (7.3)-(7.5). The derivation of the RLS in it Joseph form can be found in Appendix D, [14].

$$\hat{\boldsymbol{\theta}}_k = \hat{\boldsymbol{\theta}}_k^- + \mathbf{K}_k \left(\mathbf{y}_k - \boldsymbol{\phi}_k \hat{\boldsymbol{\theta}}_k^- \right) \tag{7.3}$$

$$\mathbf{P}_k = \left(\mathbf{I} - \mathbf{K}_k \boldsymbol{\phi}_k \right) \mathbf{P}_k^- \left(\mathbf{I} - \mathbf{K}_k \boldsymbol{\phi}_k \right) + \mathbf{K}_k \mathbf{R}_k \mathbf{K}_k^T \tag{7.4}$$

$$\mathbf{K}_k = \mathbf{P}_k^- \boldsymbol{\phi}_k \left[\boldsymbol{\phi}_k \mathbf{P}_k^- \boldsymbol{\phi}_k - \mathbf{R}_k \right]^{-1} \tag{7.5}$$

The subscript k denotes the sample, while the superscript $-$ denotes that it is priori estimates. The matrices $\mathbf{R}_k$ and $\mathbf{P}_k$ are respectively the variance matrix of the noises and the variance matrix of the difference between the actual parameters and their estimates. $\mathbf{K}_k$ is called the Kalman gain. In order to run the RLS method initial estimates of the parameter are needed. This is one of the disadvantages of the RLS method. There is as such no guarantee that the RLS method will converge to the absolute minimum. It might get stuck in a local minimum depending on the initial conditions used.

7.2 Test signal

In order to identify the parameters of the LC-filter, it is necessary create a test signal that excites all the frequencies that are needed to describe the dynamics of the filter. In system identification literature ([15] and [13]) it is commonly suggested that white random Gaussian noise is used, because it contains all frequencies.

This approach works fine for simulations, however, in practical implementation it is not advisable to excite the frequencies near the resonance peak. For this reason it is in [16] suggested that a Pseudo Random Binary Signal (PRBS) is applied instead.

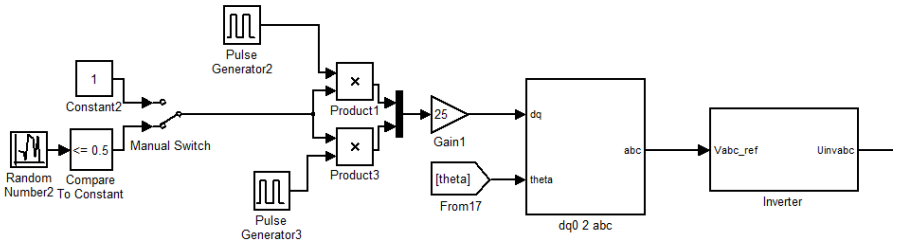

Figure 7.1: Test signal used to excite the system

The PRBS is generated as illustrated in Figure 7.1. The PRBS is generated as two PWM signals, phase shifted by π, applied as the dq-voltage reference signals for the inverter. By controlling the duty cycle of the PWM signal it can be insured that not too high currents are generated. Furthermore the amplitude of the PWM signal can be increased in accordance with the duty cycle and the measured current, as long as the measurements, imply that this is safe, thereby minimizing the effect of noise on the measurements.

7.3 Test configurations

In this section three different test configurations will be considered. All of the estimations will be based on having u_{inv} of the inverter as input. These configuration are

1. The LC-filter connected to the motor and the VSI, where only i_{inv} is measured for the estimation.
2. The LC-filter is connected to the VSI and a load resistance to discharge the capacitor, where only i_{inv} is measured for the estimation.
3. The LC-filter is not connected to anything but the VSI, where only i_{inv} is measured for the estimation.

Configuration: 1

Given that the model derived of the LC-filter and the PMSM are non-linear, it is necessary to linearize the models before they can be used in connection with the RLS method. This can be achieved by locking the motor and thus setting $\omega_e = 0$. Based on this the electrical diagram seen in Figure 7.2 can be drawn, and the transfer function of (7.9) can be set up.

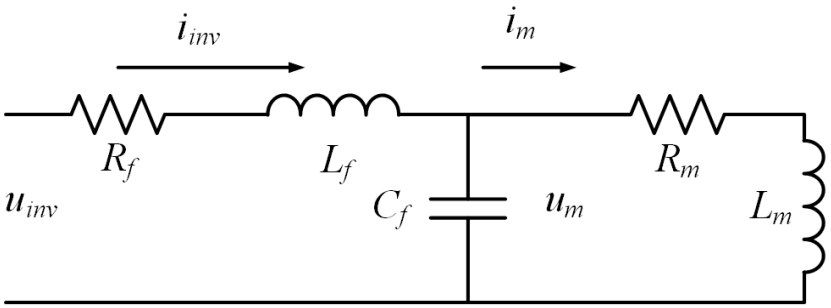

Figure 7.2: Electrical diagram of the LC-filter and PMSM at $\omega_e = 0$

$$Z_m = (R_m + sL_m) \,||\, \left(\frac{1}{C_f s}\right) \tag{7.6}$$

$$u_{inv} = i_{inv} \left(R_f + L_f s + Z_m\right) \Leftrightarrow \tag{7.7}$$

$$\frac{i_{inv}}{u_{inv}} = \frac{1}{R_f + L_f s + Z_m} \tag{7.8}$$

$$= \frac{\theta_{c:1,1} s^2 + \theta_{c:1,2} s + \theta_{c:1,3}}{s^3 + \theta_{c:1,4} s^2 + \theta_{c:1,5} s + \theta_{c:1,6}} \tag{7.9}$$

where

$$\theta_{c:1,1} = \frac{1}{L_f} \quad , \quad \theta_{c:1,2} = \frac{R_m}{L_m L_f} \quad , \quad \theta_{c:1,3} = \frac{1}{L_m L_f C_f}$$
$$\theta_{c:1,4} = \frac{R_m L_f + R_f L_m}{L_m L_f} \quad , \quad \theta_{c:1,5} = \frac{L_m + L_f + R_m R_f C_f}{L_m L_f C_f} \quad , \quad \theta_{c:1,6} = \frac{R_m + R_f}{L_m L_f C_f} \tag{7.10}$$

Given that the parameters $\theta_{c:1,1}$, $\theta_{c:1,2}$, $\theta_{c:1,3}$, $\theta_{c:1,4}$,$\theta_{c:1,5}$ and $\theta_{c:1,6}$ can be estimated and that the motor parameters already are known, the filter parameter can be found as

$$L_f = \frac{1}{\theta_{c:1,1}} \quad , \quad R_f = \theta_{c:1,2} L_m L_f \quad , \quad C_f = \frac{1}{\theta_{c:1,3} L_m L_f} \tag{7.11}$$

The parameters can then be found by converting (7.9) into the linear regression model (7.14)

$$\frac{i_{inv}}{u_{inv}} = \frac{\theta_{c:1,1} s^2 + \theta_{c:1,2} s + \theta_{c:1,3}}{s^3 + \theta_{c:1,4} s^2 + \theta_{c:1,5} s + \theta_{c:1,6}} \Leftrightarrow \tag{7.12}$$
$$\frac{1}{S^3}(\theta_{c:1,1} s^2 + \theta_{c:1,2} s + \theta_{c:1,3}) = \frac{1}{S^3}(s^3 + \theta_{c:1,4} s^2 + \theta_{c:1,5} s + \theta_{c:1,6}) \Leftrightarrow \tag{7.13}$$
$$y_{c:1} = i_{inv} = \phi^T(t)\theta_{c:1} \tag{7.14}$$
$$\phi^T_{c:1}(t) = \left[\frac{1}{s}u_{inv} \ \frac{1}{s^2}u_{inv} \ \frac{1}{s^3}u_{inv} \ -\frac{1}{s}i_{inv} \ -\frac{1}{s^2}i_{inv} \ -\frac{1}{s^3}i_{inv}\right] \tag{7.15}$$
$$\theta_{c:1} = \left[\theta_{c:1,1} \ \theta_{c:1,2} \ \theta_{c:1,3} \ \theta_{c:1,4} \ \theta_{c:1,5} \ \theta_{c:1,6}\right]^T \tag{7.16}$$

However, by looking at the bode plot, Figure 7.3, of the continuous and discrete transfer functions from (7.9) based on the parameter found in Appendix D, some of the dynamic appear near the sampling frequency, which for the setup is 5 KHz. For this reason it is not physical possible to find the proper parameter that fit the model.

This is also verified by testing the configuration under ideal condition, meaning noise, with the LS method. The LS method should here yield perfect results given that the sample frequency is high enough cover all the dynamics sufficiently.

Configuration: 2

In this configuration the LC-filter is connected to a resistance load, R_{load}, instead of the PMSM. For this configuration the single phased model is considered, for which the electrical diagram is illustrated in Figure 7.4.

This will give the transfer function found in (7.17)

$$\frac{i_{inv}}{u_{inv}} = \frac{\theta_{c:2,1} s + \theta_{c:2,2}}{s^2 + \theta_{c:2,3} s + \theta_{c:2,4}} \tag{7.17}$$

where

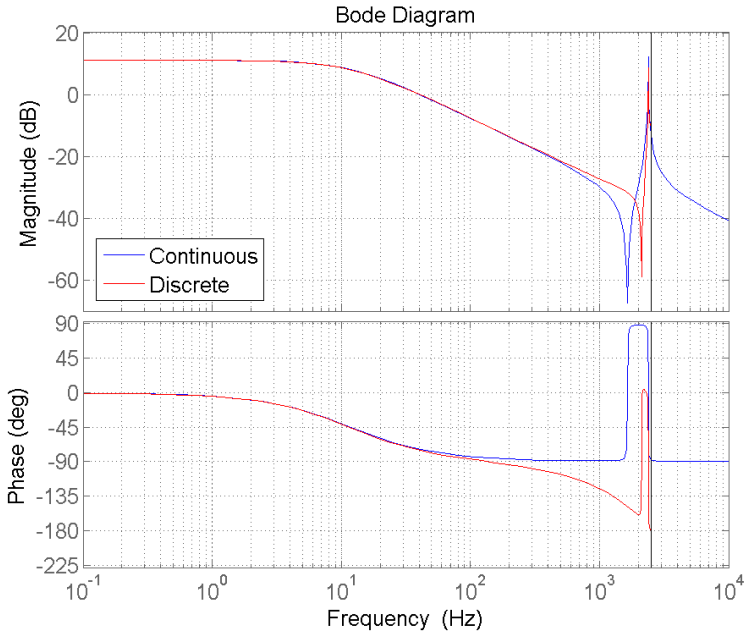

Figure 7.3: Bode plot of the continues and discrete version of (7.9)

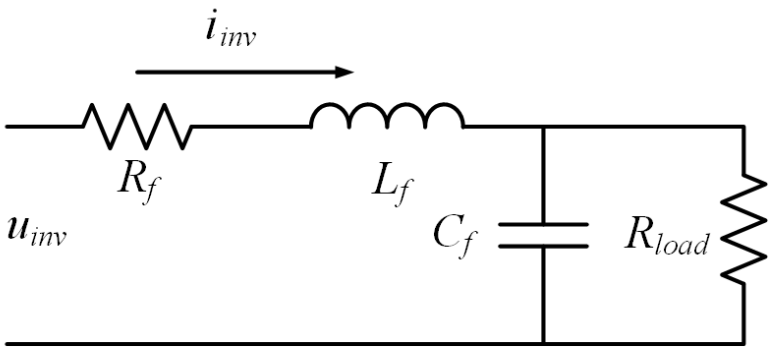

Figure 7.4: Electrical diagram of the LC-filter and a R_{load} at $\omega_e = 0$

$$\theta_{c:2,1} = \frac{R_{load}C_f}{L_f C_f R_{load}} \quad , \quad \theta_{c:2,2} = \frac{1}{L_f C_f R_{load}} \tag{7.18}$$

$$\theta_{c:2,3} = \frac{L_f + R_f C_f R_{load}}{L_f C_f R_{load}} \quad , \quad \theta_{c:2,4} = \frac{R_f + R_{load}}{L_f C_f R_{load}} \tag{7.19}$$

(7.17) can then be set up as the linear regression model (7.20)

$$y_{c:2} = i_{inv} = \phi_{c:2}^T(t)\theta_{c:2} \tag{7.20}$$

$$\phi_{c:2}^T(t) = \left[\frac{1}{s}u_{inv} \ \frac{1}{s^2}u_{inv} \ -\frac{1}{s}i_{inv} \ -\frac{1}{s^2}i_{inv}\right] \tag{7.21}$$

$$\theta_{c:2} = [\theta_{c:2,1} \ \theta_{c:2,2} \ \theta_{c:2,3} \ \theta_{c:2,4}]^T \tag{7.22}$$

R_{load} must, then, be chosen such that the current running through it is not too high based on the test signal that is used for exerting the all the frequencies. In other words a R_load with a high value is desirable, however, if the current is too small the signal-to-noise ratio (SNR) be too small to be well for identification.

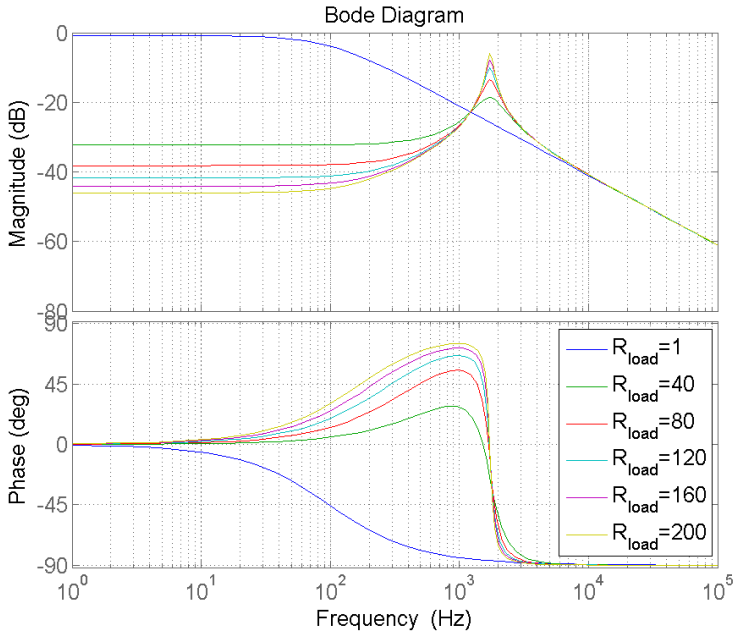

Figure 7.5: Bode plots of (7.17) with R_{load} varying in the range [1;200] ohm

In Figure 7.5 and 7.6 are shown the bode plots of the continuous and discrete versiona of the transfer function of (7.17) respectively with R_{load} varying in the range $[1; 200]$ ohm. As can be observed, there exists a resonance peak near the sampling frequency. The amplitude of this resonance peak is increased as R_{load} is increased. For this reason a low value of R_{load} is desirable.

Performing the ideal condition LS check showed that it is not possible to achieve the correct parameters, no matter the chosen value of R_{load}. Therefore this approach is disregarded as well.

Configuration: 3

In this configuration, the LC-filter is not attached to anything but the inverter. After the test signal has been applied a switch, connected to ground, is used to discharge the capacitors as a safety measure. For this configuration, the single phased model is considered, for which the electrical

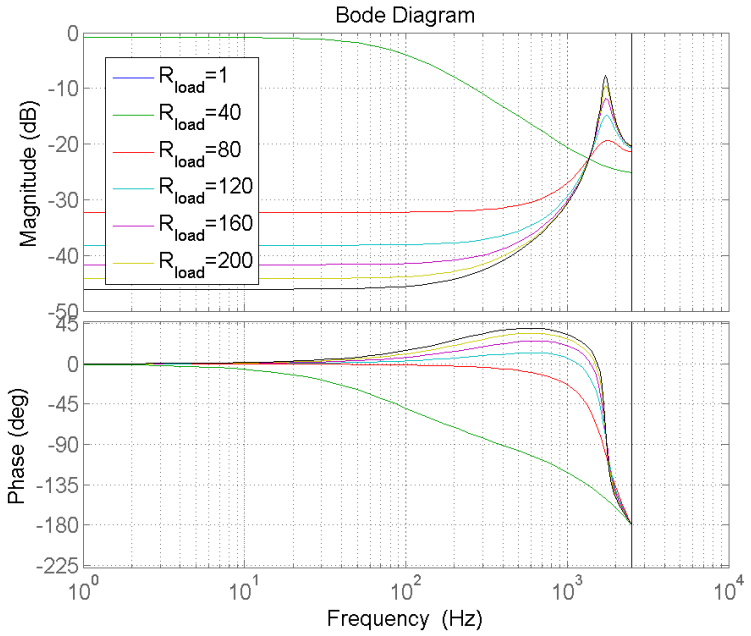

Figure 7.6: Bode plots of the discrete version of (7.17) with R_{load} varying in the range [1;200] ohm

diagram is illustrated in Figure 7.7.

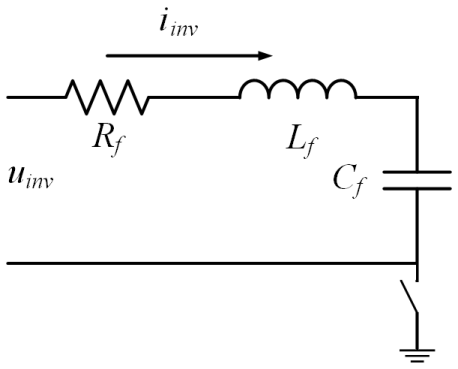

Figure 7.7: Electrical diagram of Configuration:3

The transfer function for this configuration may be found in (7.23).

$$\frac{i_{inv}}{u_{inv}} = \frac{\theta_{c:3,1}s}{s^2 + \theta_{c:2,2}s + \theta_{c:2,3}} \tag{7.23}$$

where

$$\theta_{c:3,1} = \frac{1}{L_f} \quad , \quad \theta_{c:3,2} = \frac{R_f}{L_f} \quad , \quad \theta_{c:3,3} = \frac{1}{L_f C_f} \tag{7.24}$$

The linear regression model may then be set up as

$$y_{c:3} = i_{inv} = \phi_{c:3}^T(t)\theta_{c:3} \tag{7.25}$$

$$\phi_{c:3}^T(t) = \left[\frac{1}{s}u_{inv} \;\; -\frac{1}{s}i_{inv} \;\; -\frac{1}{s^2}i_{inv}\right] \tag{7.26}$$

$$\theta_{c:3} = [\theta_{c:3,1} \;\; \theta_{c:3,2} \;\; \theta_{c:3,3}]^T \tag{7.27}$$

The parameter can then be found as

$$L_f = \frac{1}{\theta_{c:3,1}} \quad , \quad R_f = \theta_{c:3,2}L_f \quad , \quad C_f = \frac{1}{L_f\theta_{c:3,3}} \tag{7.28}$$

Applying the ideal condition LS method check for this approach provides the correct results. There is, however, one assumption that needs to be made in order to achieve correct result. This assumption is that the discrete version of the integrals in the regressor, $\phi^T(t)$, can be calculated at a higher sample frequency than the 5 kHz sampling frequency of the output signal of the inverter. This assumption is also made in the ideal condition LS method for configuration: 1 and 2, however, they still yielded incorrect results. In Figure 7.8 the discrete and the continues integral of i_{inv} are shown.

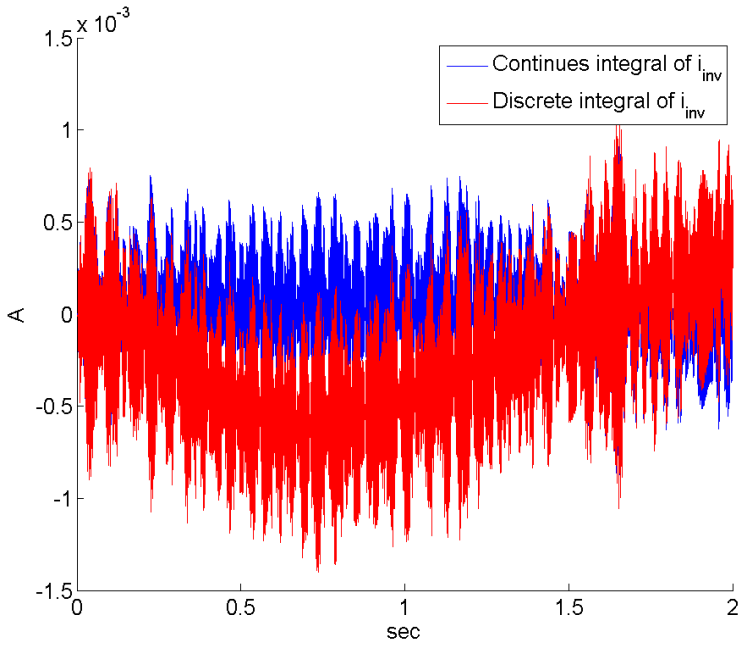

Figure 7.8: Continues and discrete integral i_{inv}

This assumption can be practically implemented by having input and output sampling run at two different frequencies. In case it becomes a problem of computation time, the integral calculation can also be moved to a dedicated DSP, which only has task of calculating these integrator

terms. The DS1103 PPC would then ever 2ms pull the integral information from the dedicated DSP.

This strategy, however, only works in the ideal case where no noise is taken into consideration, as will be explained and shown in the following.

The RLS method in this configuration uses the linear regression model found in (7.29), where the noise from i_{inv} is accounted for.

$$y_{c:3} = i_{inv} = \phi_{c:3}^T(t)\theta_{c:3} + e_{c:3} \tag{7.29}$$

$$\phi_{c:3}^T(t) = \left[\frac{1}{s}u_{inv} \;\; -\frac{1}{s}i_{inv} \;\; -\frac{1}{s^2}i_{inv}\right] \tag{7.30}$$

$$\theta_{c:3} = [\theta_{c:3,1} \;\; \theta_{c:3,2} \;\; \theta_{c:3,3}]^T \tag{7.31}$$

The variance matrix $R_{c:3}$ is thus given by

$$R_{c:2} = E[e_{c:3}e_{c:3}^T] \tag{7.32}$$

The noise from the measurement of i_{inv} is, thus, as mentioned taken into account, however, the noise that propagates into the integrators in the form shown in (7.33), is not accounted for.

$$\frac{1}{s}(i_{inv} + e_{c:3}) \quad , \quad \frac{1}{s^2}(i_{inv} + e_{c:3}) \tag{7.33}$$

This effectively means that integral term in the regressor, $\phi(t)$, will be incorrect. This will also be the case for the integral term of u_{inv}, if any extra noise is introduced between the inverter and the filter.

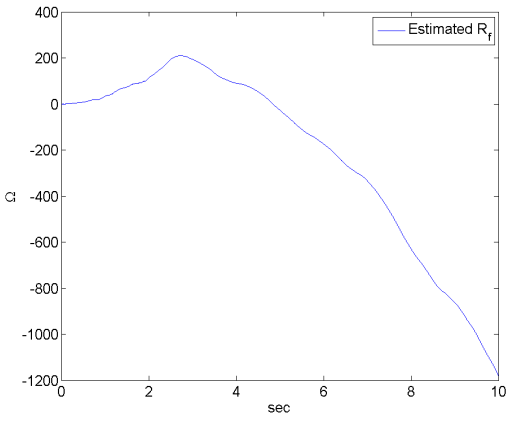

Figure 7.9: RLS estimate obtained for R_f

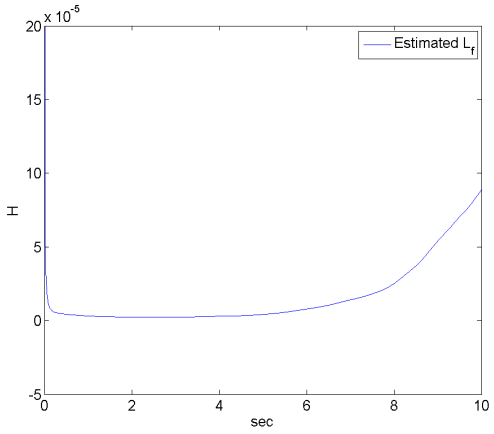

Figure 7.10: RLS estimate obtained for L_f

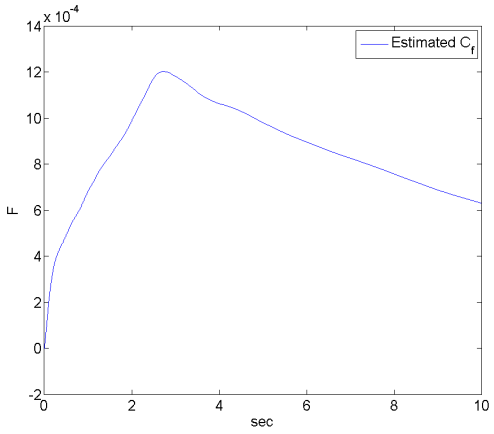

Figure 7.11: RLS estimate obtained for C_f

In Figures (7.9)-(7.11) are shown the simulated results of RLS method applied to Configuration: 3, the noise added to u_{inv} and i_{inv} has a variance that is 1% of the variance of these signal with the added noise. As can be observed even at 1% estimated parameters do not converge to the desired results.

For this reason, the approach with having the integrators in the regressor is disregarded as well. It is hereby not concluded that the RLS method cannot be used for estimating the parameters, but the another approach then converting the differential equations into a linear regression model with the integrator terms in the regressor is needed.

Another approach could be to look at the power spectrum of the currents and based on this identify the resonance peak of the filter for identification of the parameters. However, due to time limitation, this is not done in the project.

Chapter 8

Control of the PMSM and LC-filter

In this chapter the control structure used for the control system is present, then the decoupling of the differential equations investigated. The Internal Model Controller (IMC) is present as it is used for the controller in the various loop. The controllers are made discrete and checked for stability. Finally the simulation of the controller has a whole is done, and from this observations are made.

8.1 Control Structure

The model of the LC filter and the PMSM is in total composed of the following 7 differential equation.

$$\frac{d\omega_e}{dt} = \frac{3}{2J} N_{pp}^2 \lambda_{pm} i_q \tag{8.1}$$

$$u_{md} = R_m i_{md} + L_m \frac{di_{md}}{dt} - \omega_e L_m i_{mq} \tag{8.2}$$

$$u_{mq} = R_m i_{mq} + L_m \frac{di_{mq}}{dt} + \omega_e \left(L_m i_{md} + \lambda_{pm} \right) \tag{8.3}$$

$$u_{invd} = R_f i_{invd} + L_f \frac{di_{invd}}{dt} - \omega_e L_f i_{invq} + u_{md} \tag{8.4}$$

$$u_{invq} = R_f i_{invq} + L_f \frac{di_{invq}}{dt} + \omega_e L_f i_{invd} + u_{mq} \tag{8.5}$$

$$i_{invd} = C_f \frac{du_{md}}{dt} - \omega_e C_f u_{mq} + i_{md} \tag{8.6}$$

$$i_{invq} = C_f \frac{du_{mq}}{dt} + \omega_e C_f u_{md} + i_{mq} \tag{8.7}$$

As can be observed from the electrical torque equation

$$\tau_e = \frac{3}{2} N_{pp} \lambda_{pm} |\mathbf{i_{mdq}}| \sin \alpha \tag{8.8}$$

The maximum torque is achieved by having all of the motor current, $\mathbf{i_{mdq}}$, reside solely in the q-axis and thus leaving $i_{md} = 0$. This current control strategy is called the Maximum Torque Per Ampere (MTPA) strategy. In order to control $\mathbf{i_{mdq}}$ from the inverter it is, however, also necessary to control the voltage over the motor, $\mathbf{u_{mdq}}$, and the current into the filter, $\mathbf{i_{invdq}}$. The chosen control structure is a multiple loop cascade structure as illustrated in Figure 8.1. This approach is used in [16].

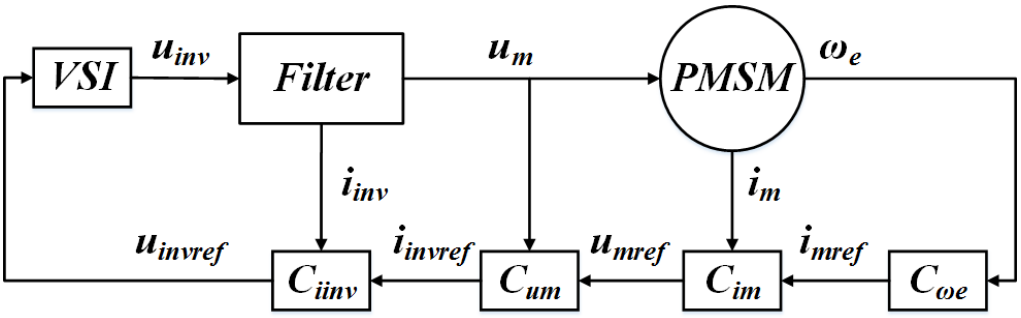

Figure 8.1: Control Structure

8.2 Decoupling

To achieve control of all of the various loops, it is necessary to remove or reduce the effect of the cross coupling terms for the d- and q-axes of i_m, u_m and i_{inv}. In (8.2)-(8.7) are given the 6 cross coupled differential equations representing the PMSM and the LC-filter, the corresponding cross coupling terms are given by (8.9)-(8.14) in the same order.

$$x_{i_{md}} = -\omega_e L_m i_{mq} \tag{8.9}$$

$$x_{i_{mq}} = \omega_e \left(L_m i_{md} + \lambda_{pm}\right) \tag{8.10}$$

$$x_{i_{invd}} = -\omega_e L_f i_{invq} + u_{md} \tag{8.11}$$

$$x_{i_{invq}} = \omega_e L_f i_{invd} + u_{mq} \tag{8.12}$$

$$x_{u_{md}} = -\omega_e C_f u_{mq} + i_{md} \tag{8.13}$$

$$x_{u_{mq}} = \omega_e C_f u_{md} + i_{mq} \tag{8.14}$$

Decoupling the differential equations the following 6 transfer functions can be set up.

$$p_{i_{md}} = \frac{i_{md}}{u_{md} - x_{i_{md}}} = \frac{1}{L_m s + R_m} \tag{8.15}$$

$$p_{i_{mq}} = \frac{i_{mq}}{u_{mq} - x_{i_{mq}}} = \frac{1}{L_m s + R_m} \tag{8.16}$$

$$p_{i_{invd}} = \frac{i_{invd}}{u_{invd} - x_{i_{invd}}} = \frac{1}{L_f s + R_f} \tag{8.17}$$

$$p_{i_{invq}} = \frac{i_{invq}}{u_{invq} - x_{i_{invq}}} = \frac{1}{L_f s + R_f} \tag{8.18}$$

$$p_{u_{md}} = \frac{u_{md}}{i_{invd} - x_{u_{md}}} = \frac{1}{C_f s} \tag{8.19}$$

$$p_{u_{mq}} = \frac{u_{mq}}{i_{invq} - x_{u_{mq}}} = \frac{1}{C_f s} \tag{8.20}$$

As can be observed the 6 transfer functions are in principal only representing 2 different types of transfer functions, namely

$$p_{i_y} = \frac{1}{L_x s + R_x} \tag{8.21}$$

$$p_{u_{mdq}} = \frac{1}{C_f s} \tag{8.22}$$

where L_x represents L_f and L_m respectively, and R_x represents R_f and R_m, while the subscript i_y represent i_{invdq} and i_{mdq}. The non-bold variables with the subscripts dq, here represent either their d- or q-axis components.

For the i_{invdq}-loop the decoupling is simply done by adding or subtracting the cross coupling from the control effort as shown in Figure 8.2

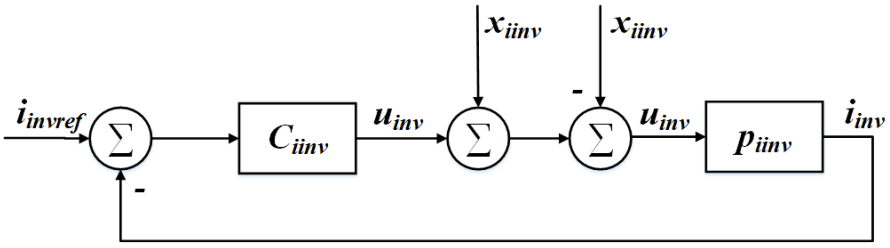

Figure 8.2: i_{invdq}-loop

In a normal cascade loop structure, it is common design procedure to make the outer loop roughly 5 times slower than the inner loop, in that way the dynamics of the inner loop can be regarded as simply a system with a gain of 1. However, when applying the same decoupling strategy to i_{mdq} and u_{mdq} it is important not just to make the outer loops 5 times slower than their respective inner loops, but instead also account for the dynamics of the decoupling terms. The scaling factor, between speed of the inner loop and the outer loop, will in the following be denoted κ. The relationship between the decoupling term the inner loop is illustrated in Figure 8.3.

As can be seen by observing the cross coupling terms (8.9)-(8.9) is both a cross coupling

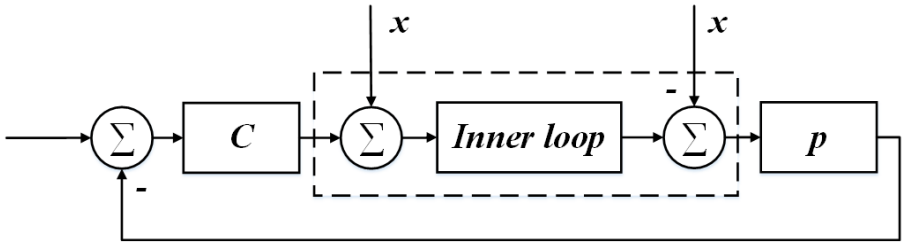

Figure 8.3: outer-loop decoupling

between the d- and q-axes of each loop, but it is also a coupling effect of outer loops from the same axis to their inner loops. A diagram of the full controlled system with all its loops and couplings and decouplings can be found in Appendix D.2.

8.3 Internal model Controller

For the design of the controller for the different loops, it is chosen to go with the Internal Model Control design approach, [17]. This is done partly because it provides an easy way of tuning the controller, which also will come in handy when implementing it on the real setup. Furthermore, it adds the possibility of online modifying the controller based on online parameter identification. The latter is specifically not done in this project, but the possibility is kept open. The concept of the IMC is illustrated in Figure 8.4.

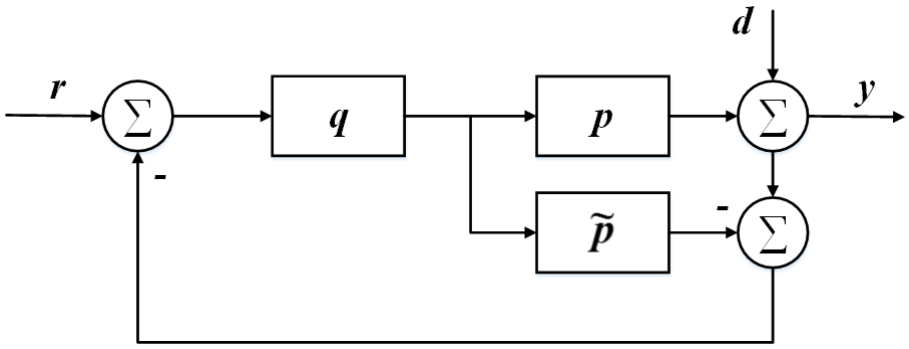

Figure 8.4: IMC structure

Instead of feeding back the output of the system, the error, between the measured output and the output of the assumed model of the system, is fed back. As shown in Figure 8.5 the IMC structure can be reconfigured into a classical control structure where the measured output of the system is fed back.

The relationship between the q and c controllers are given by

$$c = \frac{q}{1 - \tilde{p}q} \quad , \quad q = \frac{c}{1 + \tilde{p}c} \tag{8.23}$$

The output of the system can be expressed by the sensitivity function ϵ and the complementary sensitivity function η as seen in (8.24)

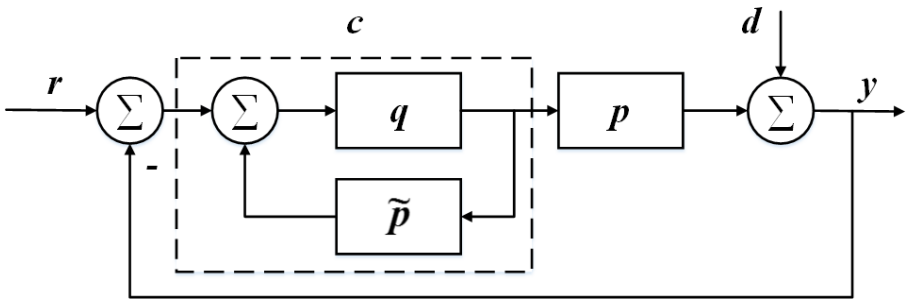

Figure 8.5: IMC structure reconfigured to classical control structure

$$y = \frac{pq}{1 + q(p - \tilde{p})} r + \frac{1 - \tilde{p}q}{1 + q(p - \tilde{p})} d = \eta r + \epsilon d \tag{8.24}$$

If it is assumed that the model perfectly fits the system, meaning $p = \tilde{p}$, then (8.24) can be rewritten as

$$y = \tilde{\eta} r + \tilde{\epsilon} d = \tilde{p}qr + (1 - \tilde{p}q)d = \tilde{\eta} r + (1 - \tilde{\eta})d \tag{8.25}$$

Assuming that $d = 0$ then it can be seen that $\tilde{\eta}$ expresses the close loop function of the controlled system. Given that the disturbance is present then it can be seen that the disturbance is diminished by $\tilde{\eta} d$.

In order for the IMC structure to be stable, it is required that both p and q are stable, assuming $p = \tilde{p}$. Besides q being stable, it is also required that q is proper. By proper is meant that (8.26) is finite.

$$\lim_{|s| \to 0} q(s) \tag{8.26}$$

If $\lim_{|s| \to \infty} |q(s)| = 0$, q is said to be strictly proper. A transfer function is strictly proper, if the order of the denominator is greater than that of the numerator. For equal order denominator and numerator the q is said to be semi-proper. In the following design procedure it is assumed that the system controlled has no non-minimum phase elements, meaning no time delay and no zeros in the right half-plane. Then, given that $\tilde{q} = \tilde{p}^{-1}$ and $q = \tilde{q} f$ the closed loop function $\tilde{\eta}$ can be written as

$$\tilde{\eta} = \tilde{p}\tilde{q}f = f \tag{8.27}$$

where

$$f = \frac{1}{(\lambda s + 1)^n} \tag{8.28}$$

n must be chosen such that q is a proper transfer function.

8.4 Current Loop Controllers

As seen mentioned all the decoupled current loops, i_{invd}, i_{invq}, i_{md}, i_{mq} in principal need to control the same type of system, merely with different parameters

$$p_{i_y} = \frac{1}{L_x s + R_x} \tag{8.29}$$

The controller q_{i_y} can thus be given as

$$q_{i_y} = \tilde{p}_{i_y}^{-1} f = (L_x s + R_x) \frac{1}{(\lambda_{i_y} s + 1)^n} \tag{8.30}$$

It can be seen that q_{i_y} is a proper transfer function for $n > 1$. For this project it is chosen to set $n = 1$. This in done, because as will be seen, this will make the controller have the form of a classical PI controller. The PID structure is in industry a much used controller. This will therefore make it easier to implement in industry where box controllers exist that are specifically set up for the PID control structure. The closed loop transfer function $\tilde{\eta}_{i_y}$ is thus given by

$$\tilde{\eta}_{i_y} = \frac{1}{(\lambda_{i_y} s + 1)} \tag{8.31}$$

Using the relationship between q and c found in (8.23) the regular controller c_{i_y} can be derived as (8.32), and as can be observed it is merely is a regular PI controller.

$$c_{i_y} = \frac{L_x s + R_x}{\lambda_{i_y} s} = \frac{L_x}{\lambda_{i_y}} + \frac{R_x}{\lambda_{i_y}} \frac{1}{s} \tag{8.32}$$

The i_{invdq}-loop is designed such that the rise time, t_r, for the step response of $\tilde{\eta}_{i_{invdq}}$ is determined by

$$t_r = 5T_s \tag{8.33}$$

thus making $\lambda_{i_{invdq}}$ given by (8.34), where $ln9$ defines the rise time as 90% of the steady state value.

$$\lambda_{i_{invdq}} = \frac{t_r}{\ln 9} \tag{8.34}$$

As mentioned in order to ignore the dynamics of i_{invdq} and the decoupling of the u_{mdq}-loop, the u_{mdq}-loop need to be at least κ times slower than the i_{invdq}-loop, and in turn the i_{mdq}-loop κ times slower than that of the u_{mdq}-loop. The time constant for the i_{mdq}-loop is thus given by

$$\lambda_{i_{mdq}} = \kappa^2 \frac{t_r}{\ln 9} \tag{8.35}$$

With all the model parameters, R_f, R_m, L_f and L_m being positive integers it can easily be seen that p_{i_y} and q_{i_y} both are stable, hence making the close loop $\tilde{\eta}_{i_y}$ also stable.

8.5 Motor Voltage Loop and Speed Loop controllers

In the same manor that decoupled currents are characterized by the same type of system, so are the motor voltage loops and the speed loop, namely a free integrator system as

$$p_y = \frac{K_x}{s} \tag{8.36}$$

where K_x represents $\frac{1}{C_f}$ and $\frac{3}{2J} N_{pp} \lambda_{pm}$ respectively for the motor voltage loop and the speed loop, while the subscript y represents u_{mdq} and ω_e. The controller q_y can hence be set up as

$$q_y = \tilde{p}_y^{-1} f = \frac{s}{K_x} \frac{1}{(\lambda_{i_y} s + 1)^n} \tag{8.37}$$

In order for q_y to be proper it is necessary that $n > 1$. It is here once again chosen to set $n = 1$, the reason is here the same as for the current loop controllers. The closed loop transfer function $\tilde{\eta}_y$ is thus given by

$$\tilde{\eta}_y = \frac{1}{(\lambda_y s + 1)} \tag{8.38}$$

Using the relationship between q and c found in (8.23) the regular controller c_y can be derived as (8.39), and as can be seen it is merely is a regular P controller.

$$c_{i_y} = \frac{1}{\lambda_y K_x} \tag{8.39}$$

As in direct derived in the previous section the time constant for the u_{mdq} loops are given by

$$\lambda_{u_{mdq}} = \kappa \frac{t_r}{\ln 9} \tag{8.40}$$

while it for the speed loop is given by

$$\lambda_{\omega_e} = \kappa^3 \frac{t_r}{\ln 9} \tag{8.41}$$

As it can be seen p_y is marginal stable and q_y is semi-proper and stable, as all the model parameter are positive, hence close loops are also stable. This can simply also be checked by seeing if $\tilde{\eta}_y$ is stable.

8.5.1 The effect of torque load

The free integrator of the system will ensure that any output disturbance or noise will not affect the steady state of the controlled closed loop, meaning no steady state error will be present. However, in the case of an input disturbance as the torque load for the speed loop, as illustrated in Figure 8.6, this is a different matter.

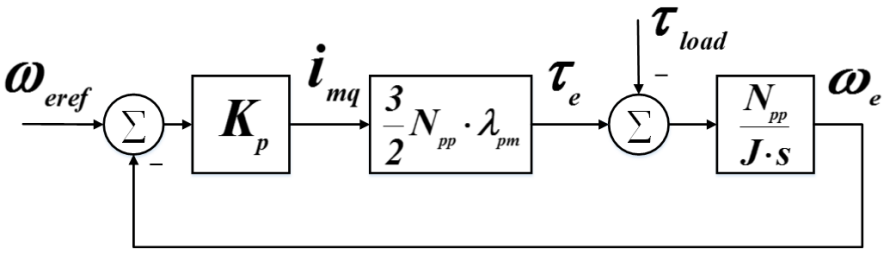

Figure 8.6: Speed loop with torque load

For this reason it is chosen to modify the speed loop as illustrated in Figure 8.7.

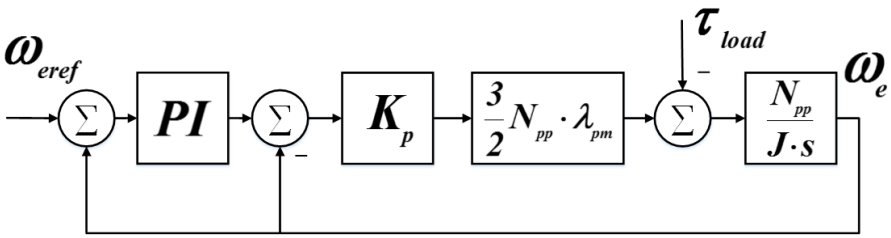

Figure 8.7: Cascade Speed loop with torque load

The introduction of the PI controller will remove the steady state error caused by the torque load. With $\tilde{\eta}_{\omega_e}$ being a first order system, the same design procedure as for the current controller can be used finding the control parameter. The desired time constant for the PI speed loop will remain the same, hence by observing (8.32) the PI controller will be given as

$$c_{i_y} = \frac{\lambda_{\omega_e} s + 1}{\lambda_{\omega_e} s} = 1 + \frac{1}{\lambda_{\omega_e}} \frac{1}{s} \tag{8.42}$$

8.6 Discrete controllers

For discretization the zero-order-hold method is used which yields the discrete PI controller found in (8.43) in parallel form. The P control, being independent of time, simple remains the same.

$$K_p + K_i \frac{T_s}{z - 1} \tag{8.43}$$

It is furthermore necessary to check if the discrete controls still yield stable closed loops. This can simply be done by checking the poles of the discretized transfer functions of $\tilde{\eta}_{i_{mdq}}$, $\tilde{\eta}_{u_{mdq}}$, $\tilde{\eta}_{i_{invdq}}$ and $\tilde{\eta}_{\omega}$ which are provided in (8.44)-(8.47). It is here decided to make the controllers with $\kappa = 10$ and $t_r = 10$, the argument for this can be found in section 8.7.

$$z_{\tilde{\eta}_{i_{invdq}}} = 0.64439 \tag{8.44}$$

$$z_{\tilde{\eta}_{u_{mdq}}} = 0.95700 \tag{8.45}$$

$$z_{\tilde{\eta}_{i_{mdq}}} = 0.99562 \tag{8.46}$$

$$z_{\tilde{\eta}_{\omega_e}} = 0.99956 \tag{8.47}$$

As can be seen all the discrete poles are placed inside the unit circle, hence all the discrete closed loops are also stable. Given the design of the PI control for the speed loop it will also have its pole at $z_{\tilde{\eta}_{\omega_e}}$.

8.7 Simulation of control and observations

In Figure 8.8 is shown the step response of $\tilde{\eta}_{\omega_e}$ and the step response of ω_e given the full cascade loop structure including the decoupling. As can be seen they deviate from each other. This deviation can be caused by the fact that the decoupling is done with inner loops in between as discussed in section 8.2.

In Figure 8.9 are shown the outputs from the inner loops and their reference input signals given the step response from Figure 8.8.

Through simulation it is found that the effects of the inner loop upon the speed loop seem to be neglectable for $\kappa > 10$, for this particular setup, the scientific reasoning for why 10 specifically is not found this project, and hence bears further investigation. In Figure 8.10 is shown the speed step response with κ taking the values, 5, 8, 10 and 15.

It is through simulation also found that changing t_r from the i_{invdq}-loop, the inner most loop, does not seem to affect the effects the inner loop dynamics on the dynamics of the speed loop.

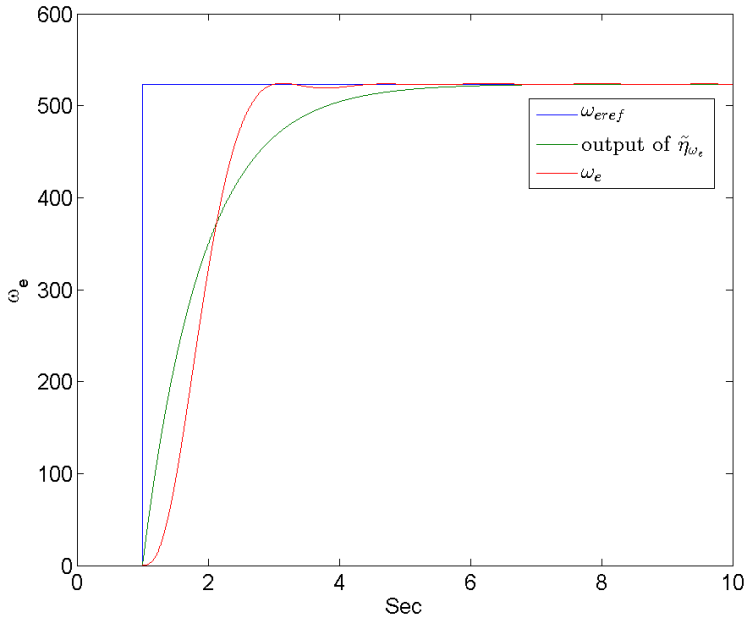

Figure 8.8: Step response of the speed-loop

This is illustrated in Figure 8.11 where t_r takes the values $t_r = 3T_s$, $t_r = 5T_s$, $t_r = 10T_s$, here $\kappa = 10$.

From this is it could also be reasoned that changing T_s could also be a way of decreasing the time constant of the speed loop, which given that the response of speed loop may seem a bit slow with $\kappa = 10$. This, however, is of cause application specific, but it does minimize the number of applications this can be used for. Changing T_s, however, also has its limitation. If T_s is set to low it may conflict with the time needed for doing all the calculations, and furthermore T_s also needs to account for the switching deadtime in the VSI.

If the outer loops such as ω_e and $i_m dq$ are not controlled, it will equate to κ being too small and thus the dynamics will propagate into the inner loops such as u_{mdq} and i_{mdq}. This is the reason why simulations showing the step response of the u_{mdq}-loop and the i_{mdq}-loop, where not made. These can therefore also not be tested as solely using the described control approach.

Based on the observations stated above it is decided to set $\kappa = 10$ and $t_r = 10$. In Figures 8.12-8.14 are shown the responses of the step of the i_{inv}-loop, the u_m-loop and the i_m-loop, respectively, compared with the step responses of their desired closed-loop transfers function, $\tilde{\eta}$.

And as can be seen the i_{inv}-loop is fairly close to its $\eta_{\tilde{i_{inv}}}$ step response. The slight difference here is associate with the fact that the coupling is continuous while the decoupling is discrete. The u_m-response, however, is far from similar to, its $\eta_{\tilde{u_m}}$ step response where as the i_m-loop again manages to have less of an overshoot. The reason for the deviation of the u_m-loop especially, is contributed to the fact that the dynamic of the outer loops affects this loop, because the are not controlled.

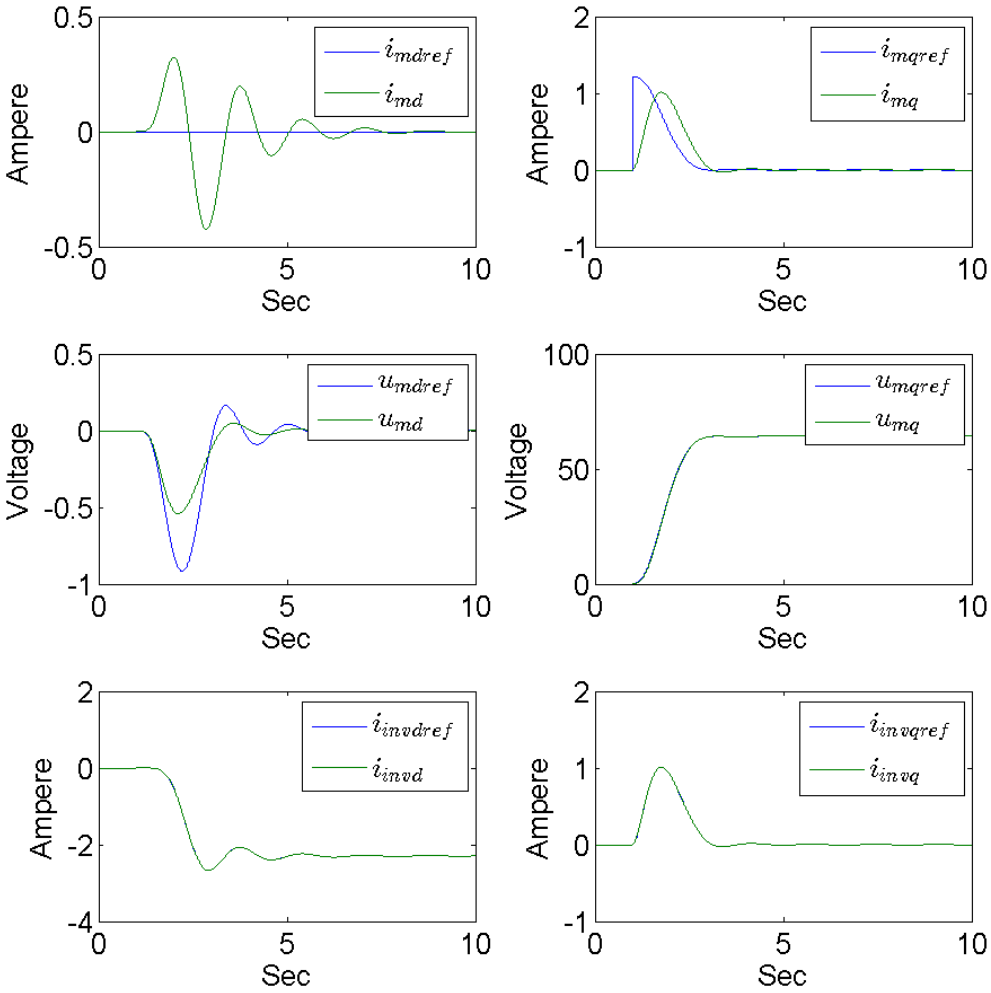

Figure 8.9: Response of the inner loop to the step response from Figure 8.8

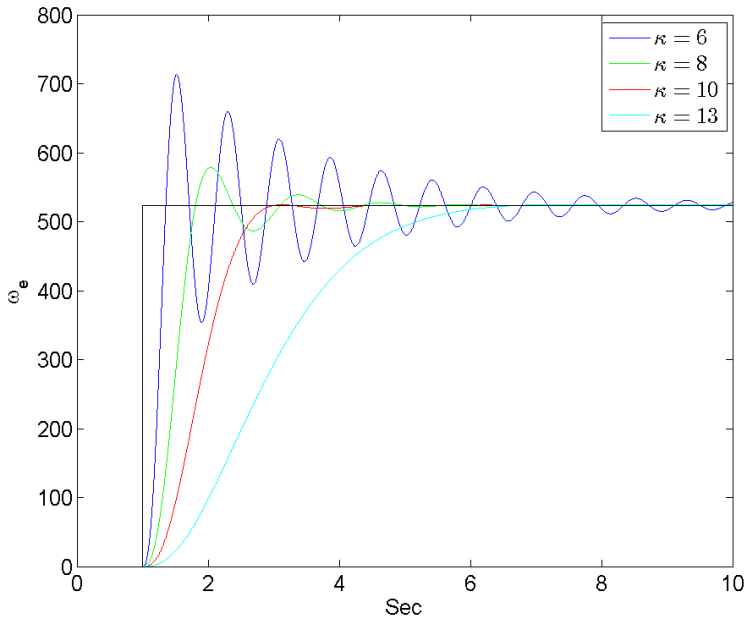

Figure 8.10: Speed step response with varying values of κ

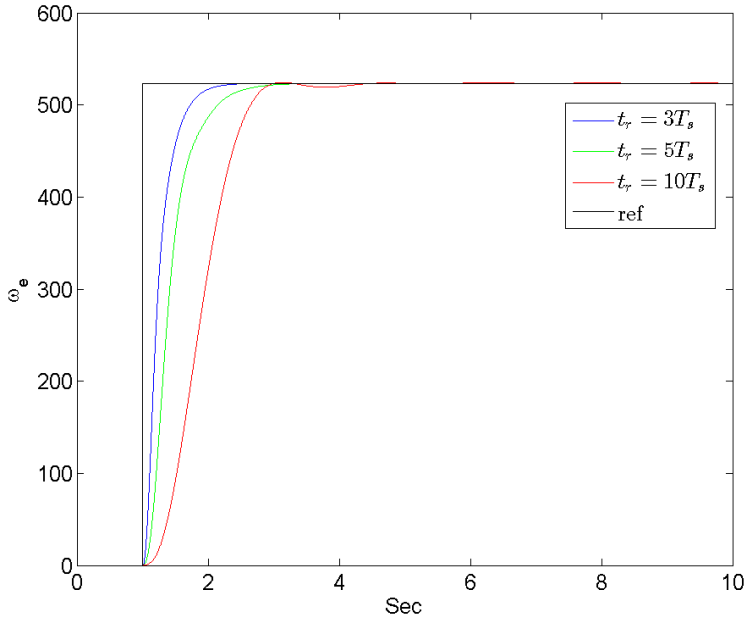

Figure 8.11: Cascade Speed loop with torque load

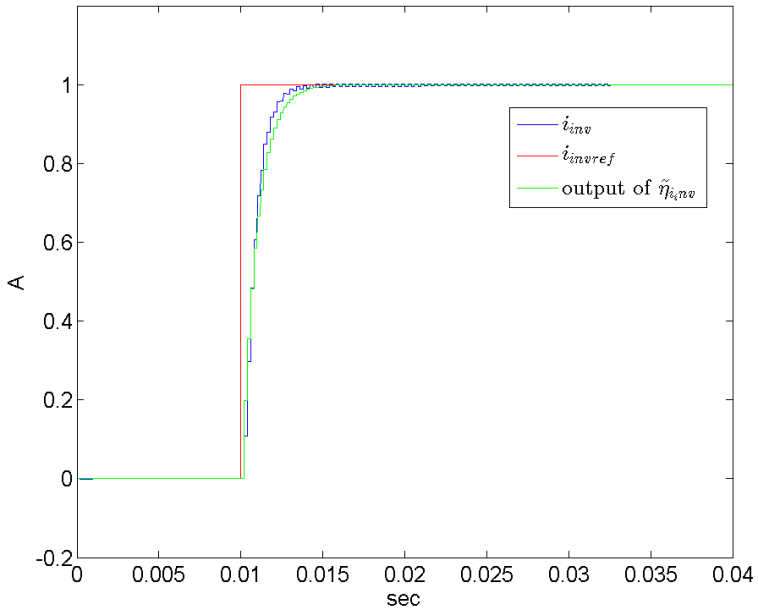

Figure 8.12: The step response of the controlled i_{inv}-loop

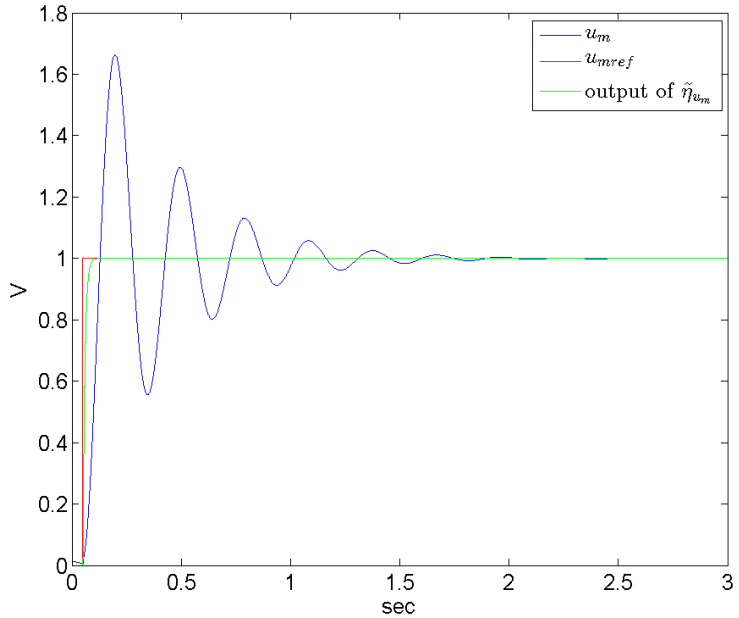

Figure 8.13: The step response of the controlled u_m-loop

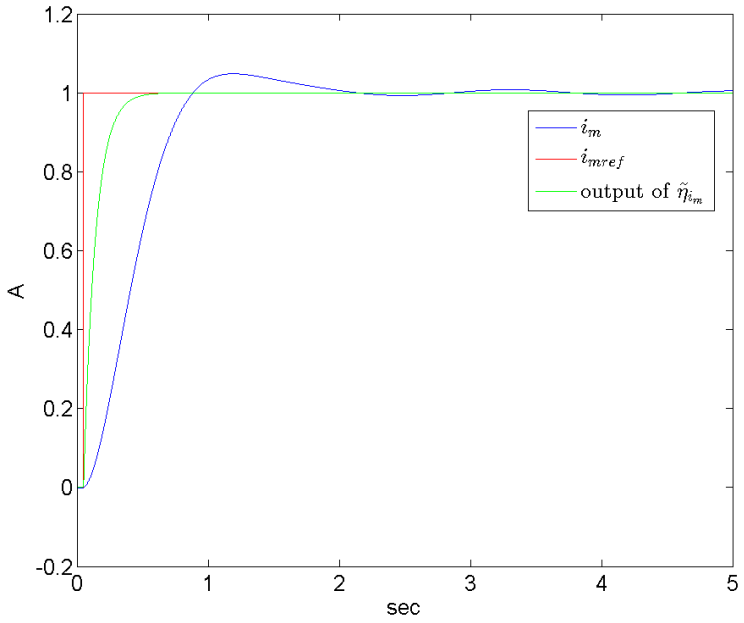

Figure 8.14: The step response of the controlled i_m-loop

Chapter 9

Test of the controller for the PMSM

Due to time issues only the i_{inv} is tested and verified under a certain condition. This condition is related to the fact that a good measurement of the motor voltage is not achieved, thus making it impossible to perform the decoupling of the i_{inv}-loop described in Section 8.2. For this reason, it is decided to set the reference of the $i_{invq} = 0$, thereby effectively setting $\omega_e = 0$ and thus removing the speed dependent terms of the couplings. The only coupling that then effects i_{invd} is u_{md}, which could not be measured properly for verification. However, in Figure 9.1 the simulated response of the i_{invd}-loop is shown, with only the u_{md}-coupling present, compared with the measured i_{invd}, and as can be seen the dynamics are very much alike. In Figure 9.2(a) and 9.2(b) are shown the measured i_{invq} and ω_m, and as can be observed they are zero as stated, or very close to it.

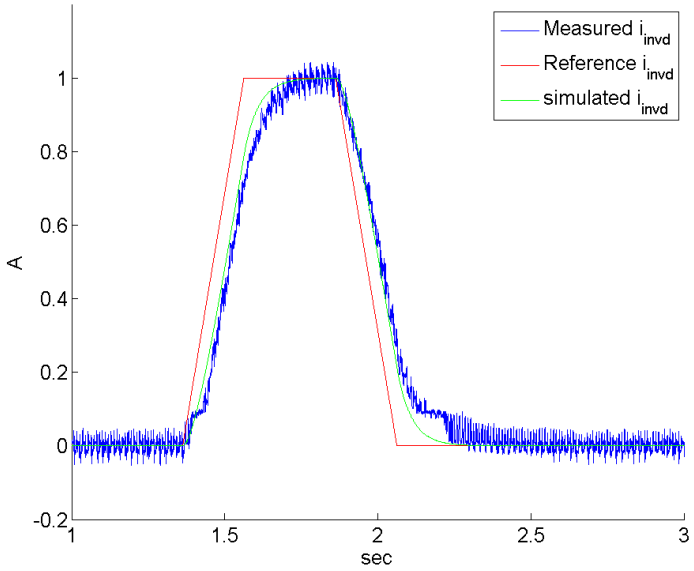

Figure 9.1: Cascade Speed loop with torque load

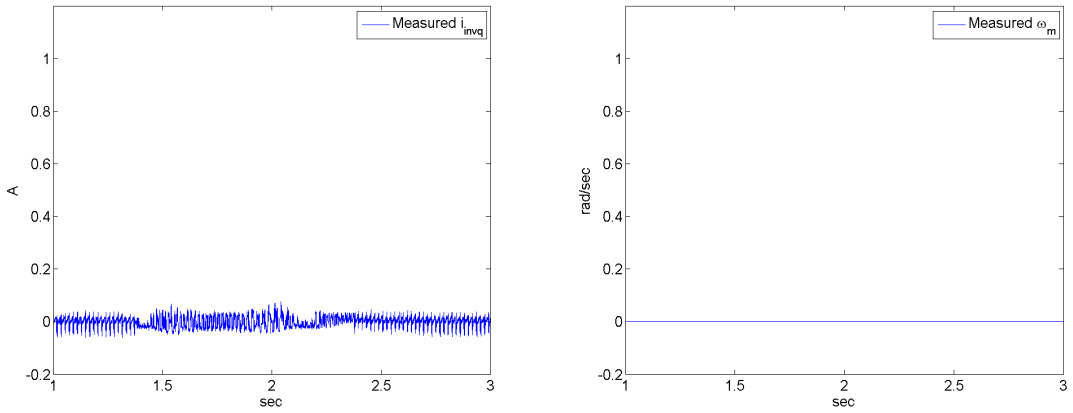

(a) i_{invq} (b) ω_m

Figure 9.2: Measured i_{invq} and ω_m with $i_{invqref} = 0$

It is, thus, also verified that the model of the filter are correct. With regards to the model of the PMSM itself there is referred to Appendix D.2, where a model verification of the PMSM itself is carried out. With a verified LC-filter model and a verified PMSM model it is thus claimed, that if the measurement problem is fixed, the proposed controllers should in theory all work.

Chapter 10

Conclusion

A model of the PMSM and the LC-filter have been successfully implemented in MATLAB's Simulink and verified experimentally. A model of the VSI using SVPWM has also been implemented and the negative effects of the VSI on the PMSM have been investigated.

The three main negative effects, that have been investigated, were:

- The cause of bearing currents that wear on the bearings.
- The ringing overshoot voltages that occur due to long leads between the motor and the VSI and cause isolation stresses in the stator windings
- The generation of magnetic caused vibration that are caused by the switching frequency and its harmonics.

Each of these can be a major issue and are highly undesirable, but can all be solved by introducing a filter between the PMSM and the VSI.

In order to identify the parameters of the LC-filter, the RLS method was investigated as an option under three different test configuration scenarios. Using a similar formulation approach for all three.

Firstly, the configuration scenarios are tested to see, if the LC-filter parameters could be obtained using merely the LS method under the assumption that no noise was present. The first two failed the check because it was determined that their dynamics are too close to the sampling frequency of 5 kHz. The third one, however, also ended up being disregarded. Not because of the configuration scenario, but because it was discovered that the approach used was not able account for the presence of noise, as first assumed, and thus was unable to converge to the correct parameters. The noise added was merely of the magnitude of 1% compared to the primary signals. For the reasons stated above, none the test configurations were experimentally carried out in the lab.

The FOC-like control structure is developed, controlling each of the states: inverter currents, motor currents, motor voltages and the speed of the motor. These states are controlled in a

multiple cascade structure consisting in total of 7 loops. For each of the loops a Internal Model Controller is developed.

It is, however, found that the way in which they are attempted to be decoupled, was dependent of the scaling relation between the speed of the inner and outer loops, in a manner that is more complex than first assumed.

It is observed that changing the response time of the inverter current loop is the easiest way of changing the response time of the speed loop. It was found that a good response was obtained with a scaling relation between the response time of the various loops of approximately 10 or larger.

Due to complications and time issues, the measurement of the motor voltage was not obtained correctly, which meant that only the inverter current loop could be experimentally verified and that only under the assumption that no decoupling was made. The results obtain, however, were similar to those provided through the simulation. So further work is needed to prove control strategy works in reality. But given the verifications of the model of the PMSM and the model of the LC-filter, it is likely that it will work, if the measurement problem is solved.

For future work it could be of interest to investigate if it would the a better approach to identify the LC-filter parameter, by looking at the power sprectrum, and hereby identifying the resonance peak of the filter. Furthermore it would be desirable to find a better way of decoupling than the one used.

Appendix A

Induction matrices derived

In this appendix the induction matrices $\mathbf{L_{mabc}}$ and $\mathbf{L_{mdq0}}$ are derived. As mentioned in chapter 4 the self- and mutual inductances of the stator windings are dependent of the rotor position. Given its dependency to the rotor position, the inductance can be described as a periodic function by a Fourier series.

$$L(\theta_e) = L_{a_0} + L_{a_1}\cos\theta_e + L_{b_1}\sin\theta_e + L_{a_2}\cos(2\theta_e) + L_{b_2}\sin(2\theta_e) \tag{A.1}$$

where third order and above components are not considered, besides they are comparably insignificant. Two constraints can be set up for the inductance, namely that it behaves as an even function, $L(\theta_e) = L(-\theta_e)$, thus removing all sine terms, and secondly that $L(\theta_e) = L(\theta_e + \pi)$ thus reducing (A.1) to

$$L(\theta_e) = L_{a_0} + L_{a_2}\cos(2\theta_e) \tag{A.2}$$

utilizing that the less airgap there is, the higher the inductance will be. The maximum inductance, L_{aad}, and the minimum inductances, L_{aaq}, can be found at $\theta_e = 0$ and $\theta_e = \frac{\pi}{2}$ respectively.

$$L(0) = L_{aad} = L_{a_0} + L_{a_2} \tag{A.3}$$
$$L\left(\frac{\pi}{2}\right) = L_{aaq} = L_{a_0} - L_{a_2} \tag{A.4}$$

The inductances L_{aad} and L_{aaq} are introduced because these can more easily be identified through measurements. Through the trigonometric relation $\cos(2\theta_e) = \cos^2\theta_e - \sin^2\theta_e$ and the defined inductances L_{aad} and L_{aaq} the induction function (A.2) can be rewritten to

$$L(\theta_e) = L_{aaq}\sin^2\theta_e + L_{aad}\cos^2\theta_e \tag{A.5}$$

Through vector projection the self- and mutual-inductances can be written as

$$L_{xy}(\theta_e) = L_{aaq}\left(\Re\left(\frac{e^{j\theta_q}}{e^{j\theta_x}}\right)\Re\left(\frac{e^{j\theta_q}}{e^{j\theta_y}}\right)\right) + L_{aad}\left(\Re\left(\frac{e^{j\theta_d}}{e^{j\theta_x}}\right)\Re\left(\frac{e^{j\theta_d}}{e^{j\theta_y}}\right)\right) \tag{A.6}$$

The subscript x and y represent the phases a, b and c. The angles θ_d, θ_q, θ_a, θ_b and θ_c are given by

$$\theta_d = \theta_e \ , \ \theta_q = \theta + \frac{\pi}{2} \ , \ \theta_a = 0 \ , \ \theta_b = -\frac{2\pi}{3} \ , \ \theta_c = \frac{2\pi}{3} \tag{A.7}$$

The self- and mutual-inductances are thus given as

$$L_{aa}(\theta_e) = L_{aaq}\sin^2\theta_e + L_{aad}\cos^2\theta_e \tag{A.8}$$

$$L_{bb}(\theta_e) = L_{aaq}\sin^2\left(\theta_e - \frac{2\pi}{3}\right) + L_{aad}\cos^2\left(\theta_e - \frac{2\pi}{3}\right) \tag{A.9}$$

$$L_{cc}(\theta_e) = L_{aaq}\sin^2\left(\theta_e + \frac{2\pi}{3}\right) + L_{aad}\cos^2\left(\theta_e + \frac{2\pi}{3}\right) \tag{A.10}$$

$$L_{ab}(\theta_e) = L_{aaq}\sin\theta_e\sin\left(\theta_e - \frac{2\pi}{3}\right) + L_{aad}\cos\theta_e\cos\left(\theta_e - \frac{2\pi}{3}\right) \tag{A.11}$$

$$L_{ac}(\theta_e) = L_{aaq}\sin\theta_e\sin\left(\theta_e + \frac{2\pi}{3}\right) + L_{aad}\cos\theta_e\cos\left(\theta_e + \frac{2\pi}{3}\right) \tag{A.12}$$

$$L_{bc}(\theta_e) = L_{aaq}\sin\left(\theta_e - \frac{2\pi}{3}\right)\sin\left(\theta_e + \frac{2\pi}{3}\right) + L_{aad}\cos\left(\theta_e - \frac{2\pi}{3}\right)\cos\left(\theta_e + \frac{2\pi}{3}\right) \tag{A.13}$$

The inductance matrix is thus given by (A.14), where the leakage inductances also are added

$$\mathbf{L_{mabc}}\left(\theta_e\right) = \begin{bmatrix} L_{aa}(\theta_e) & L_{ab}(\theta_e) & L_{ac}(\theta_e) \\ L_{ab}(\theta_e) & L_{bb}(\theta_e) & L_{bc}(\theta_e) \\ L_{ab}(\theta_e) & L_{bc}(\theta_e) & L_{cc}(\theta_e) \end{bmatrix} + \begin{bmatrix} \lambda_{aal} & 0 & 0 \\ 0 & \lambda_{bbl} & 0 \\ 0 & 0 & \lambda_{ccl} \end{bmatrix} \tag{A.14}$$

The dq0 inductance matrix can through some mathmatical manipulation be found as

$$\mathbf{L_{mdq0}} = T\mathbf{L_{mabc}}\left(\theta_e\right)T^{-1} \Leftrightarrow \tag{A.15}$$

$$\mathbf{L_{mdq0}} = \begin{bmatrix} L^*_{md} + L_{ls} & 0 & 0 \\ 0 & L^*_{mq} + L_{ls} & 0 \\ 0 & 0 & L_{ls} \end{bmatrix} = \begin{bmatrix} L_{md} & 0 & 0 \\ 0 & L_{mq} & 0 \\ 0 & 0 & L_{ls} \end{bmatrix} \tag{A.16}$$

where

$$L^*_{md} = \frac{3}{2}L_{maad} \ , \ L_{md} = L^*_{md} + L_{ls} \tag{A.17}$$

$$L^*_{mq} = \frac{3}{2}L_{maaq} \ , \ L_{mq} = L^*_{mq} + L_{ls} \tag{A.18}$$

Appendix B

SVPWM

In this appendix formulation of the SVPWM is described and derived.

The SVPWM employs space vectors to calculate switching time. Given the fact that there are 6 switches, there exist the possibility of 2^3 different switch states. Having the upper of a switch pair active, while the its lower is inactive is defined as 1. The opposite is defined as 0.

The 6 states $100 - 101$ are defined as active states, while the states 000 and 111 are defined as the zero states. In the zero states there are no potential difference that can induce a current.[1]

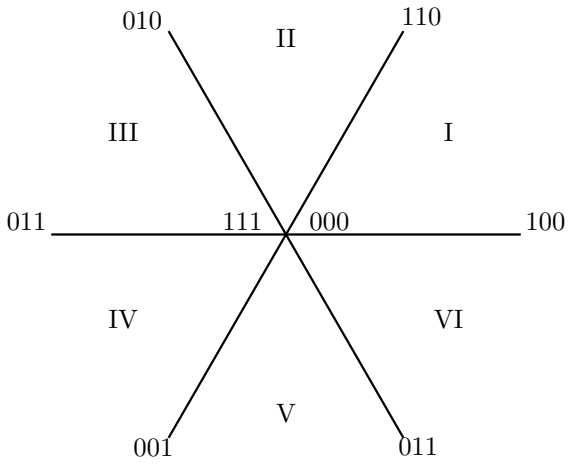

Figure B.1: The sections and states of SVPWM

In Figure B.1 is shown the three phases split up into the 6 sectors.

Compared to traditional sinusoidal modulation, SVM provides a more efficient use of the supplied DC link voltage as illustrated in Figure B.3.

For any space vector in the SVPWM hexagon of Figure B.3 it can maximum have a length of $\frac{1}{\sqrt{3}}u_{dc}$,

Any space vector in the hexagon [2] can be expressed as a sum of the two adjacent active vectors

[1] The first two paragraphs including Figure B.1 are taken directly from at previous report by the author, [23]

[2] The following until next footnote is also taken from [23], written the the author

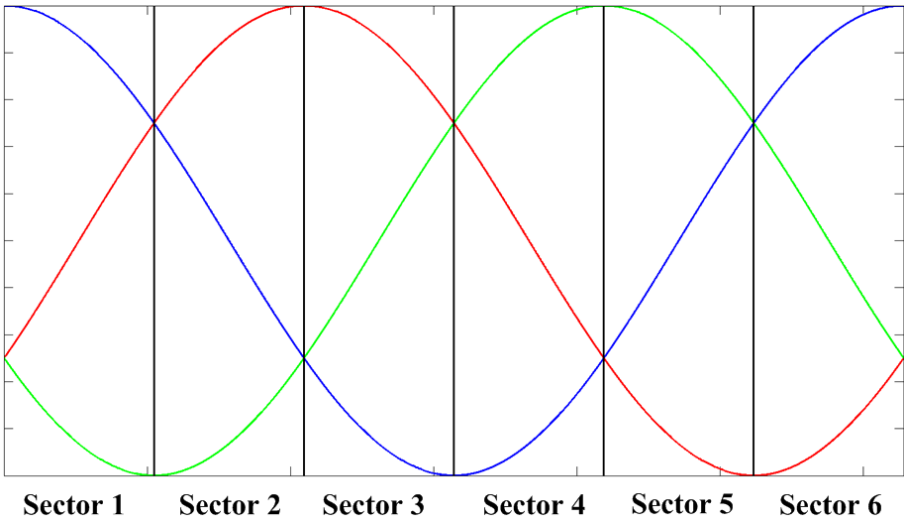

Figure B.2: The three phases split up into the three phases

of the section it is in.

$$V = c_1 V_1 + c_2 V_2 \tag{B.1}$$

c_1 and c_2 defines the time in which the inverter is in the current switch state. The total period of the pwm signal is defined by the time spent in the adjacent active vectors, T_1 and T_2, and the time spent in the zero states, T_0

c_1 and c_2 are thus defined as

$$c_1 = \frac{T_1}{T} \quad , \quad c_2 = \frac{T_2}{T} \tag{B.2}$$

T_1 and T_2 can be calculated by the following equations

$$T_1 = \frac{\sqrt{3} T_s \left|V\right|}{2 V_d c} \sin(\frac{n}{3}\pi - \theta) \tag{B.3}$$

$$T_2 = \frac{\sqrt{3} T_s \left|V\right|}{2 V_d c} \sin(\theta - \frac{n-1}{3}\pi) \tag{B.4}$$

n defines the section the space vector is in. V_{dc} is the DC-link voltage. See appendix **??** for the derivation of the equations.[3]

The remaining time of T_s that is not spent in V_1 or V_2 is spent in either the zero vector of state 000 or 111. This time is denoted as T_0 and the following relation can be set up

[3]See previous footnote

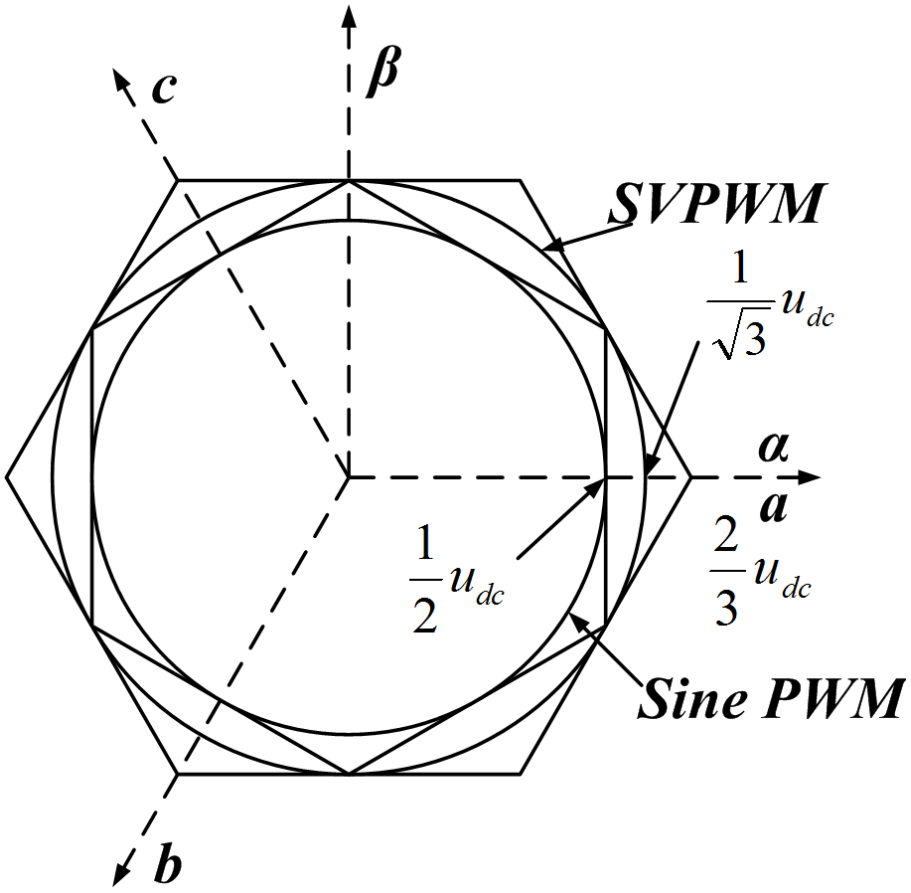

Figure B.3: SVPWM and Sine PWM use of DC link voltage

$$T_s = T_0 + T_1 + T_2 \tag{B.5}$$

In principal, T_s can be split up into any number of segments and the output set in any order desirable as long as the total time spent in the adjacent active vectors and in the zero vectors are T_1, T_2 and T_0 respectively. However, for the purpose of less THD and less switching losses the symmetric 7-segment switching sequence is chosen. In Figure B.5 is shown the PWM signal generated for all three phases for sector 1.

The time, T_0, is in the symmetric 7-segment switching sequence equally divided between the zero state vector 000 and 111.

In Figure B.6 is illustrated the various total ON-times for the different phases in each sector for a signal period, T_s. The duty cycle for each sector can be calculated as

$$D_a = T_a/T_s \quad , \quad D_b = T_b/T_s \quad , \quad D_c = T_c/T_s \tag{B.6}$$

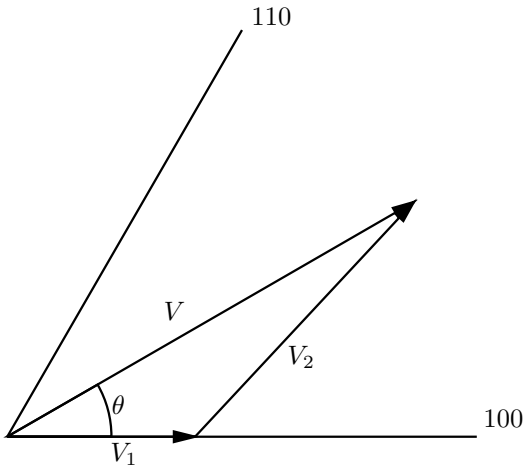

Figure B.4: Expressing the space vector via the 2 active adjacent vectors

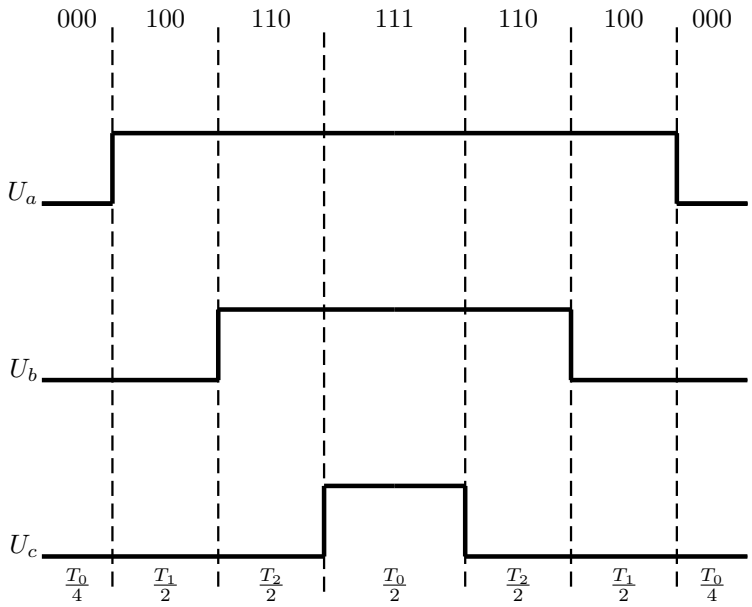

Figure B.5: The PWM signal from SVPWM for sector 1

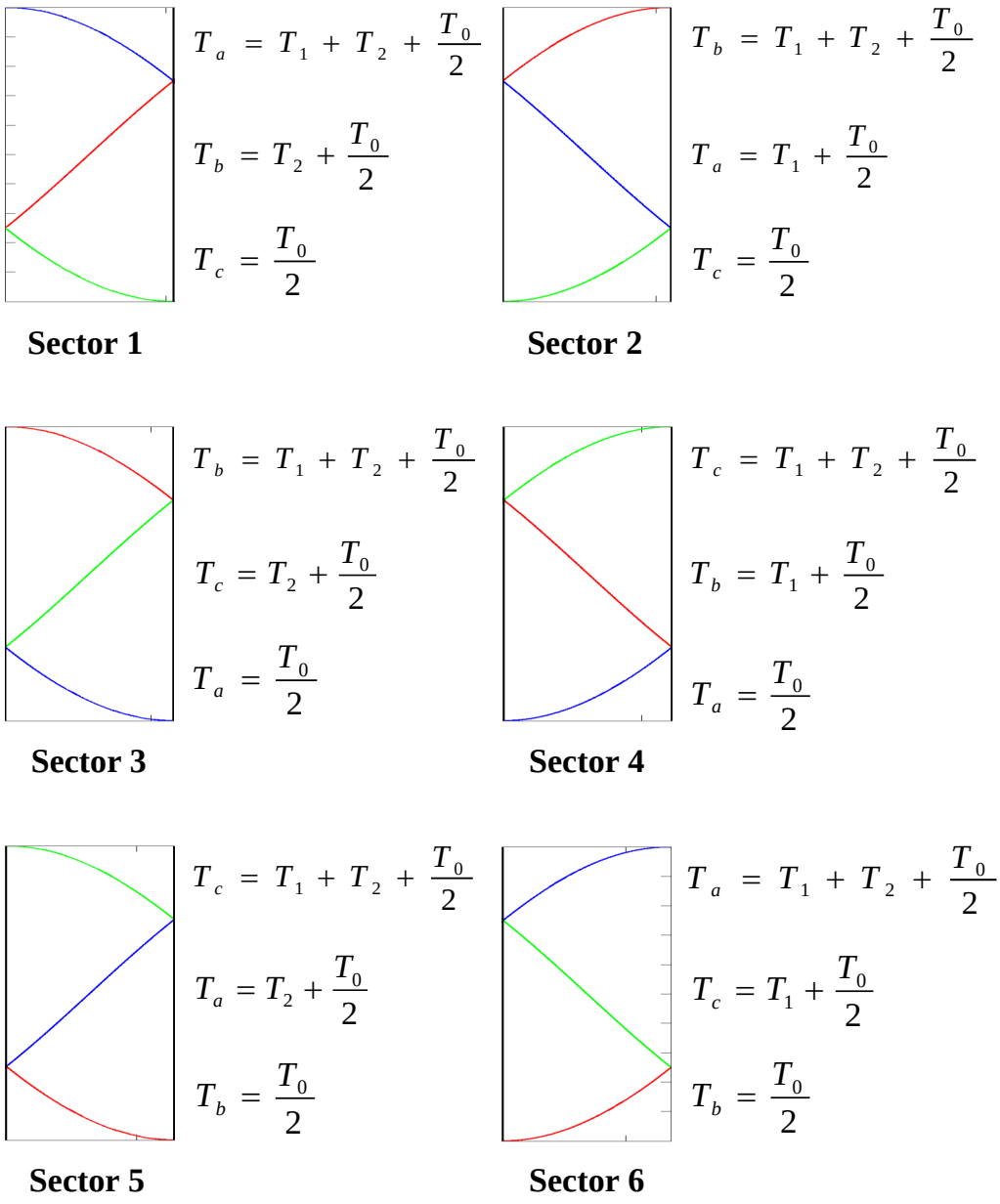

Figure B.6: Total on time for the different phases in the various sectors

Appendix C

LC-filter equations

In this appendix the dq equations for the LC-filter are derived.

In vector form the three phase voltage equation for the LC-filter may be written as

$$\mathbf{u_{invabc}} = \mathbf{R_f}\mathbf{i_{invabc}} + \frac{d}{dt}\boldsymbol{\lambda}_{\mathbf{invabc}} + \mathbf{u_{mabc}} \tag{C.1}$$

$$\boldsymbol{\lambda}_{\mathbf{invabc}} = \mathbf{L_f}\mathbf{i_{invabc}} \tag{C.2}$$

Applying the combined Park and Clark transformation, $\mathbf{T}$, the equations may be rewritten as

$$\begin{aligned}
\mathbf{T}^{-1}\mathbf{T}\mathbf{u_{invabc}} &= \mathbf{R_f}\mathbf{T}^{-1}\mathbf{T}\mathbf{i_{invabc}} + \frac{d}{dt}\left(\mathbf{T}^{-1}\mathbf{T}\boldsymbol{\lambda}_{\mathbf{invabc}}\right) + \mathbf{T}^{-1}\mathbf{T}\mathbf{u_{mabc}} \Leftrightarrow \\
\mathbf{T}^{-1}\mathbf{u_{invdq0}} &= \mathbf{R_f}\mathbf{T}^{-1}\mathbf{i_{invdq0}} + \frac{d}{dt}\left(\mathbf{T}^{-1}\boldsymbol{\lambda}_{\mathbf{invdq0}}\right) + \mathbf{T}^{-1}\mathbf{u_{mdq0}} \\
&= \mathbf{R_f}\mathbf{T}^{-1}\mathbf{i_{invdq0}} + \left(\frac{d}{dt}\mathbf{T}^{-1}\right)\boldsymbol{\lambda}_{\mathbf{invdq0}} + \mathbf{T}^{-1}\left(\frac{d}{dt}\boldsymbol{\lambda}_{\mathbf{invdq0}}\right) + \mathbf{T}^{-1}\mathbf{u_{mdq0}} \\
&= \mathbf{R_f}\mathbf{T}^{-1}\mathbf{i_{invdq0}} + \mathbf{T}^{-1}\omega_e\mathbf{J_T}\boldsymbol{\lambda}_{\mathbf{invdq0}} + \mathbf{T}^{-1}\left(\frac{d}{dt}\boldsymbol{\lambda}_{\mathbf{invdq0}}\right) + \mathbf{T}^{-1}\mathbf{u_{mdq0}} \Leftrightarrow \\
\mathbf{u_{invdq0}} &= \mathbf{R_f}\mathbf{i_{invdq0}} + \omega_e\mathbf{J_T}\boldsymbol{\lambda}_{\mathbf{invdq0}} + \frac{d}{dt}\boldsymbol{\lambda}_{\mathbf{invdq0}} + \mathbf{u_{mdq0}}
\end{aligned} \tag{C.3}$$

and for $\boldsymbol{\lambda}_{\mathbf{invabc}}$

$$\begin{aligned}
&\mathbf{T}^{-1}\mathbf{T}\boldsymbol{\lambda}_{\mathbf{invabc}} = \mathbf{L_f}\mathbf{T}^{-1}\mathbf{T}\mathbf{i_{invabc}} \Leftrightarrow \\
&\mathbf{T}^{-1}\boldsymbol{\lambda}_{\mathbf{invdq0}} = \mathbf{L_f}\mathbf{T}^{-1}\mathbf{i_{invdq0}} \Leftrightarrow \\
&\boldsymbol{\lambda}_{\mathbf{invdq0}} = \mathbf{L_f}\mathbf{i_{invdq0}}
\end{aligned} \tag{C.4}$$

The voltage equation (C.3) can now be written as

$$\mathbf{u_{invdq0}} = \mathbf{R_f}\mathbf{i_{invdq0}} + \omega_e\mathbf{J_T}\mathbf{L_f}\mathbf{i_{invdq0}} + \mathbf{L_f}\frac{d}{dt}\mathbf{i_{invdq0}} + \mathbf{u_{mdq0}} \tag{C.5}$$

In the same way the current equation for the three phase LC-filter may also be transformed

$$\begin{aligned}
\mathbf{T}^{-1}\mathbf{T}\mathbf{i}_{\mathbf{invabc}} &= \mathbf{C_f}\frac{d}{dt}\left(\mathbf{T}^{-1}\mathbf{T}\mathbf{u}_{\mathbf{invabc}}\right) + \mathbf{T}^{-1}\mathbf{T}\mathbf{i}_{\mathbf{mabc}} \Leftrightarrow \\
\mathbf{T}^{-1}\mathbf{i}_{\mathbf{invdq0}} &= \mathbf{C_f}\frac{d}{dt}\left(\mathbf{T}^{-1}\mathbf{u}_{\mathbf{invdq0}}\right) + \mathbf{T}^{-1}\mathbf{i}_{\mathbf{mdq0}} \\
&= \mathbf{C_f}\left(\left(\frac{d}{dt}\mathbf{T}^{-1}\right)\mathbf{u}_{\mathbf{invdq0}} + \mathbf{T}^{-1}\left(\frac{d}{dt}\mathbf{u}_{\mathbf{invdq0}}\right)\right) + \mathbf{T}^{-1}\mathbf{i}_{\mathbf{mdq0}} \\
&= \mathbf{C_f}\left(\mathbf{T}^{-1}\omega_e\mathbf{J_T}\mathbf{u}_{\mathbf{invdq0}} + \mathbf{T}^{-1}\left(\frac{d}{dt}\mathbf{u}_{\mathbf{invdq0}}\right)\right) + \mathbf{T}^{-1}\mathbf{i}_{\mathbf{mdq0}} \Leftrightarrow \\
\mathbf{i}_{\mathbf{invdq0}} &= \mathbf{C_f}\omega_e\mathbf{J_T}\mathbf{u}_{\mathbf{invdq0}} + \mathbf{C_f}\frac{d}{dt}\mathbf{u}_{\mathbf{invdq0}} + \mathbf{i}_{\mathbf{mdq0}} \qquad \text{(C.6)}
\end{aligned}$$

In non-vector from dq equations for the LC-filter can now be expressed as

$$u_{invd} = R_f i_{invd} - \omega_e L_f i_{invq} + L_f\frac{di_{invd}}{dt} + u_{md} \qquad \text{(C.7)}$$

$$u_{invq} = R_f i_{invq} - \omega_e L_f i_{invd} + L_f\frac{di_{invq}}{dt} + u_{mq} \qquad \text{(C.8)}$$

$$i_{invd} = -\omega_e C_f u_{mq} + C_f\frac{du_{md}}{dt} + i_{md} \qquad \text{(C.9)}$$

$$i_{invq} = -\omega_e C_f u_{md} + C_f\frac{du_{mq}}{dt} + i_{mq} \qquad \text{(C.10)}$$

Appendix D

PMSM and LC-filter parameters

Table D.1: Parameters of the PMSM

Parameter	Symbol	Value	Unit
Rated phase voltage	V_n	164	[V]
Rated current	I_n	19.5	[A]
Rated torque	τ_n	20	[Nm]
Rated speed	n_n	4500	[rpm]
Stator resistance	R_s	0.18	[Ω]
Synchronous inductance	L_d	2	[mH]
Synchronous inductance	L_q	2	[mH]
Moment of inertia	J	0.0158	[Kgm^2]
Number of pole pairs	n_{pp}	4	-
Permanent magnet peak flux linkage	$lambda_{mpm}$	0.123	[Wb]
Rated speed	ω_n	1885	[rad/s]

Table D.2: Parameters of the LC-filter

Parameter	Symbol	Value	Unit
LC-filter resistance	R_f	0.1154	[Ω]
LC-filter inductance	L_f	1.8e-3	[H]
LC-filter capacitance	C_f	4.7e-6	[F]

Appendix E

In this appendix the Least Squares method and the Recursive Least Squares method are derived.

D.1 Least Squares Method

The RLS method is an extension of the Least Squares (LS) method which therefore will be briefly derived first.

The LS method the objective of finding the least squares, as the name indicates. Specifically, the squares found in the cost function (D.2), which is the square of the error between the measured output, and the estimated output. The $\boldsymbol{\theta_p}$ that is found at the minimum of the cost function represent the parameter that makes the linear regression model best fit to the system it tries to represent.

$$V(\boldsymbol{\theta_p}, t) = \frac{1}{2}\sum_{i=1}^{t}\left(y(i) - \hat{y}(i)\right)^2 \tag{D.1}$$

$$= \frac{1}{2}\sum_{i=1}^{t}\left(y(i) - \boldsymbol{\phi}(t)^T\boldsymbol{\theta_p}\right)^2 \tag{D.2}$$

the minimum is simply found by setting the derivative with respect to $\boldsymbol{\theta_p}$ to zero.

$$\frac{dV(\boldsymbol{\theta_p}, t)}{d\boldsymbol{\theta_p}} = \sum_{i=1}^{t}\boldsymbol{\phi}(t)\left(y(i) - \boldsymbol{\phi}(t)^T\boldsymbol{\theta_p}\right) = 0 \Leftrightarrow \tag{D.3}$$

$$\hat{\boldsymbol{\theta}}_p = \left[\sum_{i=1}^{t}\boldsymbol{\phi}(i)\boldsymbol{\phi}(i)^T\right]^{-1}\sum_{i=1}^{t}\boldsymbol{\phi}(i)y(i) \tag{D.4}$$

The estimate $\hat{\boldsymbol{\theta}}_p$ is based on the entire sample space where as the RLS as mentioned is an iterative method that for each sample updates its estimate.

D.2 Recursive Least Squares Method, Joseph Form

Given that the linear regression model with the measurement noise, $\mathbf{e}_k$, is given by (D.5).

$$\mathbf{y}_k = \boldsymbol{\phi}_k \boldsymbol{\theta}_k + \mathbf{e}_k \tag{D.5}$$

It is thus desirable to find an expression that updates the estimated parameter $\hat{\boldsymbol{\theta}}_k$ based on the measured output $\mathbf{y}_k$ and the priori estimate $\hat{\boldsymbol{\theta}}_k^-$. An linear approach to such a relation is given by (D.6).

$$\hat{\boldsymbol{\theta}}_k = \mathbf{K}_k^{(*)} \hat{\boldsymbol{\theta}}_k^- + \mathbf{K}_k \mathbf{y}_k \tag{D.6}$$

Where $\mathbf{K}_k^{(*)}$ and $\mathbf{K}k$ are matrices that need to be derived.

The difference between the actual values and their estimates for $\mathbf{y}_k$ and $\boldsymbol{\theta}_k$ are denoted $\tilde{\mathbf{y}}_k$ and $\tilde{\boldsymbol{\theta}}_k$ as in (D.7) and (D.8) respectively.

$$\tilde{\mathbf{y}}_k = \mathbf{y}_k - \hat{\mathbf{y}}_k \tag{D.7}$$
$$\tilde{\boldsymbol{\theta}}_k = \boldsymbol{\theta}_k - \hat{\boldsymbol{\theta}}_k \tag{D.8}$$

Based on the principle of orthogonality (D.9) can be stated and because it is assumed that $\mathbf{e}_k$ and $\mathbf{y}_k$ are uncorrelated (D.10) can be stated.

$$E\left[\tilde{\boldsymbol{\theta}}_k \mathbf{y}_l^T\right] = 0 \tag{D.9}$$
$$E\left[\mathbf{e}_k \mathbf{y}_k\right] = 0 \tag{D.10}$$

By combining (D.5), (D.6) and (D.8) and using that $\mathbf{e}_k$ and $\mathbf{y}_k$ are uncorrelated, (D.9) can be rewritten as

$$E\left[\left(\boldsymbol{\theta}_k - \left(\mathbf{K}_k^{(*)} \hat{\boldsymbol{\theta}}_k^- + \mathbf{K}_k \left(\boldsymbol{\phi}_k \boldsymbol{\theta}_k - \mathbf{e}_k\right)\right)\right) \mathbf{y}_k^T\right] \tag{D.11}$$
$$= E\left[\left(\boldsymbol{\theta}_k - \left(\mathbf{K}_k^{(*)} \hat{\boldsymbol{\theta}}_k^- + \mathbf{K}_k \boldsymbol{\phi}_k \boldsymbol{\theta}_k - \mathbf{K}_k \mathbf{e}_k\right)\right) \mathbf{y}_k^T\right] \tag{D.12}$$
$$= E\left[\boldsymbol{\theta}_k \mathbf{y}_k^T - \mathbf{K}_k^{(*)} \hat{\boldsymbol{\theta}}_k^- \mathbf{y}_k^T - \mathbf{K}_k \boldsymbol{\phi}_k \boldsymbol{\theta}_k \mathbf{y}_k^T + \mathbf{K}_k \mathbf{e}_k \mathbf{y}_k^T\right] \tag{D.13}$$
$$= E\left[\left(\mathbf{I} - \mathbf{K}_k \boldsymbol{\phi}_k\right) \boldsymbol{\theta}_k \mathbf{y}_k - \mathbf{K}_k^{(*)} \hat{\boldsymbol{\theta}}_k^- \mathbf{y}_k^T\right] + \mathbf{K}_k E\left[\mathbf{e}_k \mathbf{y}_k^T\right] \tag{D.14}$$
$$= E\left[\left(\mathbf{I} - \mathbf{K}_k \boldsymbol{\phi}_k - \mathbf{K}_k^{(*)}\right) \boldsymbol{\theta}_k \mathbf{y}_k + \mathbf{K}_k^{(*)} \left(\boldsymbol{\theta}_k - \hat{\boldsymbol{\theta}}_k^-\right) \mathbf{y}_k^T\right] = 0 \Leftrightarrow \tag{D.15}$$
$$= E\left[\left(\mathbf{I} - \mathbf{K}_k \boldsymbol{\phi}_k - \mathbf{K}_k^{(*)}\right) \boldsymbol{\theta}_k \mathbf{y}_k\right] + \mathbf{K}_k^{(*)} E\left[\left(\boldsymbol{\theta}_k - \hat{\boldsymbol{\theta}}_k^-\right) \mathbf{y}_k^T\right] = 0 \tag{D.16}$$

Due to the orthogonality principle (D.17) can also be stated

$$E\left[\left(\boldsymbol{\theta}_k - \hat{\boldsymbol{\theta}}_k^-\right) \mathbf{y}_k^T\right] = 0 \tag{D.17}$$

Hence (D.16) can be rewritten as

$$E\left[\left(\mathbf{I}-\mathbf{K}_k\boldsymbol{\phi}_k-\mathbf{K}_k^{(*)}\right)\boldsymbol{\theta}_k\mathbf{y}_k\right]=\left(\mathbf{I}-\mathbf{K}_k\boldsymbol{\phi}_k-\mathbf{K}_k^{(*)}\right)E\left[\boldsymbol{\theta}_k\mathbf{y}_k\right]=0 \tag{D.18}$$

Which implies

$$\mathbf{I}-\mathbf{K}_k\boldsymbol{\phi}_k-\mathbf{K}_k^{(*)}=0 \tag{D.19}$$

$\mathbf{K}_k^{(*)}$ can thus be expressed terms of $\mathbf{K}_k$

$$\mathbf{K}_k^{(*)}=\mathbf{I}-\mathbf{K}_k\boldsymbol{\phi}_k \tag{D.20}$$

Inserting (D.20) into (D.6) yield the parameter update relation (D.22)

$$\hat{\boldsymbol{\theta}}_k=\left(\mathbf{I}-\mathbf{K}_k\boldsymbol{\phi}_k\right)\bar{\hat{\boldsymbol{\theta}}_k}+\mathbf{K}_k\mathbf{y}_k \tag{D.21}$$

$$=\bar{\hat{\boldsymbol{\theta}}_k}+\mathbf{K}_k\left(\mathbf{y}_k-\boldsymbol{\phi}_k\bar{\hat{\boldsymbol{\theta}}_k}\right) \tag{D.22}$$

$\mathbf{K}_k$ is called the Kalman gain. And is the same as from the well known Extended Kalman Filter (EKF). In fact the RLS is a special case of the EKF.

By inspection of (D.17) it can also be implied that

$$E\left[\left(\boldsymbol{\theta}_k-\hat{\boldsymbol{\theta}}_k\right)\hat{\mathbf{y}}_k^T\right]=0 \tag{D.23}$$

and hence

$$E\left[\left(\boldsymbol{\theta}_k-\hat{\boldsymbol{\theta}}_k\right)\tilde{\mathbf{y}}_k^T\right]=0 \tag{D.24}$$

The difference between the actual output and the estimate base on the priori estimated parameters can be expressed as

$$\tilde{\mathbf{y}}_k=\mathbf{y}_k-\boldsymbol{\phi}_k\bar{\hat{\boldsymbol{\theta}}_k}=\boldsymbol{\phi}_k\boldsymbol{\theta}_k+\mathbf{e}_k-\boldsymbol{\phi}_k\bar{\hat{\boldsymbol{\theta}}_k}=\boldsymbol{\phi}_k\bar{\tilde{\boldsymbol{\theta}}_k}+\mathbf{e}_k \tag{D.25}$$

Using (D.22) and (D.25) the difference between the actual parameters and their estimates can be expressed as

$$\boldsymbol{\theta}_k - \hat{\boldsymbol{\theta}}_k = \boldsymbol{\theta} - \left(\hat{\boldsymbol{\theta}}_k^- + \mathbf{K}_k\left(\mathbf{y}_k - \boldsymbol{\phi}_k\hat{\boldsymbol{\theta}}_k^-\right)\right) = \boldsymbol{\theta} - \hat{\boldsymbol{\theta}}_k^- - \mathbf{K}_k\left(\boldsymbol{\phi}_k\boldsymbol{\theta}_k + \mathbf{e}_k - \boldsymbol{\phi}_k\hat{\boldsymbol{\theta}}_k^-\right) \tag{D.26}$$

$$= \tilde{\boldsymbol{\theta}}_k^- - \mathbf{K}_k\left(\boldsymbol{\phi}_k\tilde{\boldsymbol{\theta}}_k^- + \mathbf{e}_k\right) = \left(\mathbf{I} - \mathbf{K}_k\boldsymbol{\phi}_k\right)\tilde{\boldsymbol{\theta}}_k^- - \mathbf{K}_k\mathbf{e}_k \tag{D.27}$$

With this the expectation of (D.24) can be rewritten as (D.30)

$$E\left[\left(\left(\mathbf{I} - \mathbf{K}_k\boldsymbol{\phi}_k\right)\tilde{\boldsymbol{\theta}}_k^- - \mathbf{K}_k\mathbf{e}_k\right)\left(\boldsymbol{\phi}_k\tilde{\boldsymbol{\theta}}_k^- + \mathbf{e}_k\right)\right] \tag{D.28}$$

$$= E\left[\left(\mathbf{I} - \mathbf{K}_k\boldsymbol{\phi}_k\right)\tilde{\boldsymbol{\theta}}_k^-\tilde{\boldsymbol{\theta}}_k^{T-}\boldsymbol{\phi}_k - \mathbf{K}_k\mathbf{e}_k\mathbf{e}_k^T\right] \tag{D.29}$$

$$= \left(\mathbf{I} - \mathbf{K}_k\boldsymbol{\phi}_k\right)E\left[\tilde{\boldsymbol{\theta}}_k^-\tilde{\boldsymbol{\theta}}_k^{T-}\right]\boldsymbol{\phi}_k - \mathbf{K}_kE\left[\mathbf{e}_k\mathbf{e}_k^T\right] \tag{D.30}$$

It is here utilized that $\tilde{\boldsymbol{\theta}}_k^-$ and $\mathbf{e}_k$ are expected to be uncorrelated. By introducing the matrices $\mathbf{P}_k$ and $\mathbf{R}_k$, where

$$\mathbf{P}_k^- = E\left[\tilde{\boldsymbol{\theta}}_k^-\tilde{\boldsymbol{\theta}}_k^{T-}\right] = E\left[\left(\boldsymbol{\theta}_k - \hat{\boldsymbol{\theta}}_k^-\right)\left(\boldsymbol{\theta}_k - \hat{\boldsymbol{\theta}}_k^-\right)^T\right] \tag{D.31}$$

$$\mathbf{R}_k = E\left[\mathbf{e}_k\mathbf{e}_k^T\right] \tag{D.32}$$

(D.30) can be rewritten as (D.34) which express the update equation of the Kalman gain.

$$\left(\mathbf{I} - \mathbf{K}_k\boldsymbol{\phi}_k\right)\mathbf{P}_k^-\boldsymbol{\phi}_k - \mathbf{K}_k\mathbf{R}_k = \mathbf{P}_k^-\boldsymbol{\phi}_k - \mathbf{K}_k\left(\boldsymbol{\phi}_k\mathbf{P}_k^-\boldsymbol{\phi}_k - \mathbf{R}_k\right) \Leftrightarrow \tag{D.33}$$

$$\mathbf{K}_k = \mathbf{P}_k^-\boldsymbol{\phi}_k\left[\boldsymbol{\phi}_k\mathbf{P}_k^-\boldsymbol{\phi}_k - \mathbf{R}_k\right]^{-1} \tag{D.34}$$

The remaining update equation for P_k, can be expressed as (D.39) by utilizing (D.27).

$$\mathbf{P}_k = E\left[\tilde{\boldsymbol{\theta}}_k\tilde{\boldsymbol{\theta}}_k^T\right] = E\left[\left(\boldsymbol{\theta}_k - \hat{\boldsymbol{\theta}}_k\right)\left(\boldsymbol{\theta}_k - \hat{\boldsymbol{\theta}}_k\right)^T\right] \tag{D.35}$$

$$= E\left[\left(\left(\mathbf{I} - \mathbf{K}_k\boldsymbol{\phi}_k\right)\tilde{\boldsymbol{\theta}}_k^- - \mathbf{K}_k\mathbf{e}_k\right)\left(\left(\mathbf{I} - \mathbf{K}_k\boldsymbol{\phi}_k\right)\tilde{\boldsymbol{\theta}}_k^- - \mathbf{K}_k\mathbf{e}_k\right)^T\right] \tag{D.36}$$

$$= E\left[\left(\mathbf{I} - \mathbf{K}_k\boldsymbol{\phi}_k\right)\tilde{\boldsymbol{\theta}}_k^-\tilde{\boldsymbol{\theta}}_k^{T-}\left(\mathbf{I} - \mathbf{K}_k\boldsymbol{\phi}_k\right)\right] + E\left[\mathbf{K}_k\mathbf{e}_k\mathbf{e}_k^T\mathbf{K}_k^T\right] \tag{D.37}$$

$$= \left(\mathbf{I} - \mathbf{K}_k\boldsymbol{\phi}_k\right)E\left[\tilde{\boldsymbol{\theta}}_k^-\tilde{\boldsymbol{\theta}}_k^{T-}\right]\left(\mathbf{I} - \mathbf{K}_k\boldsymbol{\phi}_k\right) + \mathbf{K}_kE\left[\mathbf{e}_k\mathbf{e}_k^T\right]\mathbf{K}_k^T \tag{D.38}$$

$$= \left(\mathbf{I} - \mathbf{K}_k\boldsymbol{\phi}_k\right)\mathbf{P}_k^-\left(\mathbf{I} - \mathbf{K}_k\boldsymbol{\phi}_k\right) + \mathbf{K}_k\mathbf{R}_k\mathbf{K}_k^T \tag{D.39}$$

The RLS method is then composed of the three equations (D.22), (D.34) and (D.39).

Appendix F

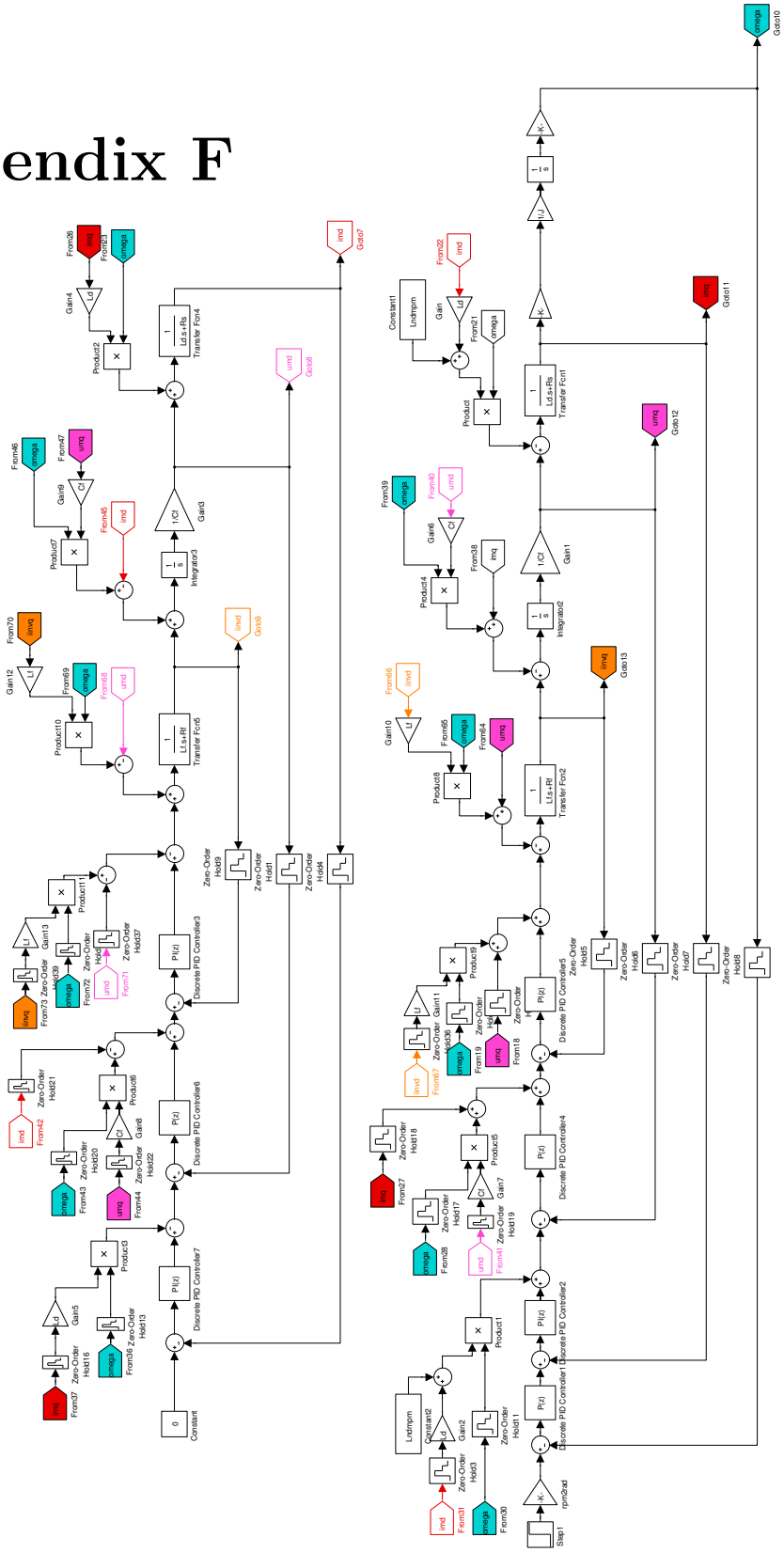

Appendix G

In this appendix[1] the simulink model of the PMSM is compared and validated up against the measured responses obtained from the real system. The PMSM is controlled by speed FOC utilizing MTPA with the parameters found in Table D.3. The datasheet parameters for the PMSM can be found in Table D.4.

Table D.3: dSPACE Controller Parameters

Controller	k_p (proportional gain)	k_i (integrator gain)
Current loop	2.7	1000
Speed loop	0.1	0.8

Table D.4: Parameters of the PMSM

Parameter	Symbol	Value	Unit
Rated phase voltage	V_n	164	[V]
Rated current	I_n	19.5	[A]
Rated torque	τ_n	20	[Nm]
Rated speed	n_n	4500	[rpm]
Stator resistance	R_s	0.18	[Ω]
Synchronous inductance	L_d	2	[mH]
Synchronous inductance	L_q	2	[mH]
Moment of inertia	J	0.48	[mKgm^2]
Number of pole pairs	n_{pp}	4	-
Permanent magnet peak flux linkage	$lambda_{mpm}$	0.123	[Wb]
Rated speed	ω_n	1885	[rad/s]

The resulting step response the simulink model using the control parameters, Table D.3, is in Figure D.1 compared with the step response of the speed for the real system using the same control parameters.

As can be seen the model yields a reasonable result compared to the real system. The slope of the step response that can be seen in the figure is due to a rate limiter, which is a safety precaution set up in the dSpace program used.

In Figures D.2(a) and D.2(b) are seen the response of i_{md} and i_{mq} respectively using the step

[1]This appendix is a modified version of a chapter from an old report by the author, [23]

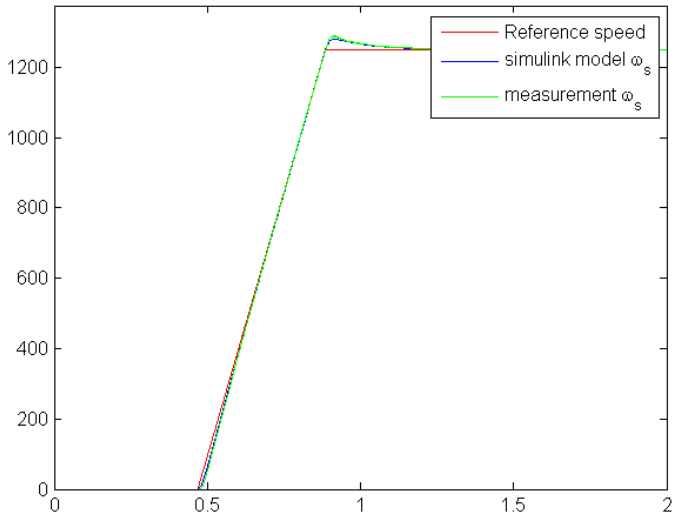

Figure D.1: Step response of the speed using the parameters of Table D.3 and D.4

of the speed, $omega_ref = 1250rpm$, from above.

Besides the measurement being noisy, the id signal is acceptable, however as can be seen in the figure D.2(b) there is here a discrepancy between the model and the real system with regard to the i_{mq} signal. This discrepancy is partly due to the fact that the inertia of the real system is larger, because it no longer only is composed of motor alone but now also is composed of what is attached to the motor. The resulting change to the inertia is shown in figure D.3, where it can be seen that the current now yields a satisfactory result.

The offset that can be seen in i_{mq} at steady state is caused by the viscous friction that is present in the real system. With $\tau_l = 0$ the viscous friction coefficient can in steady state be found as

$$\tau_{e_{ss}} = b_{fric}\omega_{m_{ss}} \Leftrightarrow b_{fric} = \frac{\tau_{e_{ss}}}{\omega_{m_{ss}}} \tag{D.40}$$

However, it is deemed that the friction is small enough to be neglected. The resulting change of inertia yields the speed response that can be found in Figure D.4.

With both current and speed of the model and the real system matching to satisfaction, the model and the controllers are found to be satisfactorily validated. The new motor parameters with the larger inertia can be found in Appendix D.

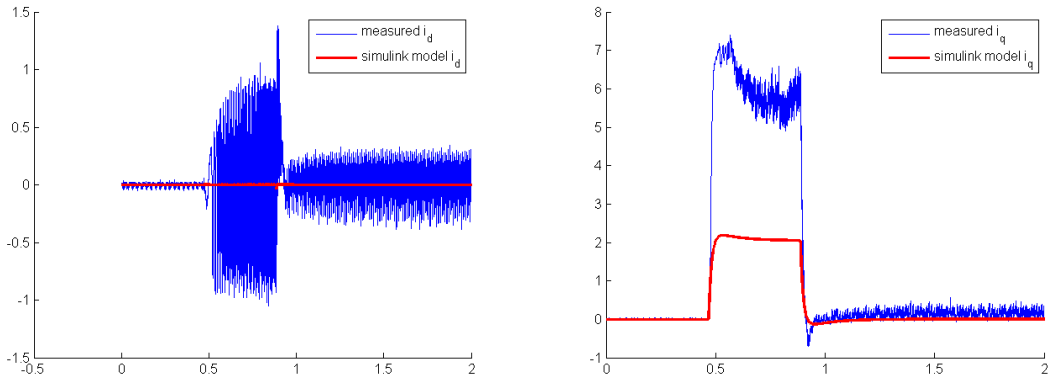

(a) i_d (b) i_q

Figure D.2: Current response from speed step ($\omega_{ref} = 1250$) (a) i_d, (b) i_q

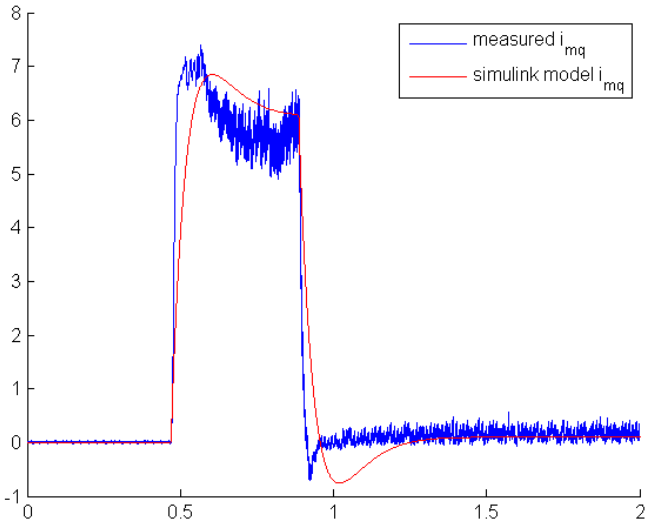

Figure D.3: i_{mq} response from speed step ($\omega_{ref} = 1250$ rpm) with new inertia

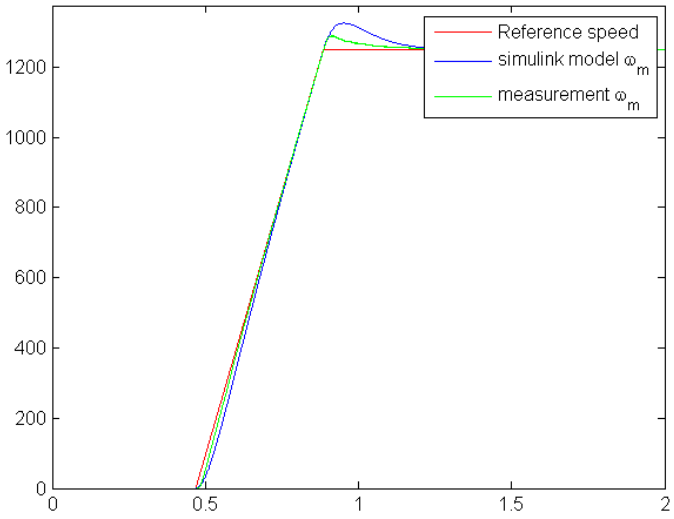

Figure D.4: Step response of the speed using the parameters of Table D.3 and D.4

Bibliography

[1] http://www.mst.dk/English/Noise/recommended_noise_limits/noise_zones/noise_zone_industry/

[2] 'System identification and diagnosis', course provided at Aalborg University

[3] Vieira, Rodrigo Padilha, Rodrigo Zelir Azzolin, and H. A. Grundling. "Parameter identification of a single-phase induction motor using RLS algorithm." Power Electronics Conference, 2009. COBEP'09. Brazilian. IEEE, 2009.

[4] Morimoto, Shigeo, Masayuki Sanada, and Yoji Takeda. "Mechanical sensorless drives of IPMSM with online parameter identification." Industry Applications, IEEE Transactions on 42.5 (2006): 1241-1248.

[5] Chen, S., T. A. Lipo, and D. Fitzgerald. "Source of induction motor bearing currents caused by PWM inverters." Energy conversion, IEEE transactions on 11.1 (1996): 25-32.

[6] Salomaki, Janne, Marko Hinkkanen, and Jorma Luomi. "Influence of inverter output filter on maximum torque and speed of PMSM drives." Industry Applications, IEEE Transactions on 44.1 (2008): 153-160.

[7] Von Jouanne, A., P. Enjeti, and W. Gray. "The effect of long motor leads on PWM inverter fed AC motor drive systems." Applied Power Electronics Conference and Exposition, 1995. APEC'95. Conference Proceedings 1995., Tenth Annual. IEEE, 1995.

[8] Output Filters Design Guide, Danfoss A/S

[9] Persson, Erik. "Transient effects in application of PWM inverters to induction motors." Industry Applications, IEEE Transactions on 28.5 (1992): 1095-1101.

[10] Sutthiphornsombat, B., A. Khoobroo, and B. Fahimi. "Mitigation of acoustic noise and vibration in permanent magnet synchronous machines drive using field reconstruction method." Vehicle Power and Propulsion Conference (VPPC), 2010 IEEE. IEEE, 2010.

[11] Yamazaki, Katsumi, and Yoshiaki Seto. "Iron loss analysis of interior permanent-magnet synchronous motors-variation of main loss factors due to driving condition." Industry Applications, IEEE Transactions on 42.4 (2006): 1045-1052.

[12] Aalborg University, Getting started with the drives laboratory with dSPACE - Users Guide, June 2011, Aalborg University, Institute of Energy Technology

[13] Torben Knudsen, Systemidentikation, AUC-PROCES-U-93-4008, Aalborg University, Januar 1993

[14] Haykin, Simon S., ed. Kalman filtering and neural networks. New York: Wiley, 2001.

[15] Keesman, Karel J. System Identification: An Introduction. Springer, 2011.

[16] Szczupak, Piotr, and M. Pacas. "Automatic identification of a PMSM drive equipped with an output LC-filter." IEEE Industrial Electronics, IECON 2006-32nd Annual Conference on. IEEE, 2006.

[17] Morari, Manfred, and Evanghelos Zafiriou. Robust process control. Morari, 1989.

[18] Lu, Kaiyuan, Peter Omand Rasmussen, and Ewen Ritchie. "A simple and general approach to determination of self and mutual inductances for AC machines." Electrical Machines and Systems (ICEMS), 2011 International Conference on. IEEE, 2011.

[19] 'Dynamic models of electrical machines', course provided at Aalborg University

[20] Zhang, Wei-Feng, and Yue-Hui Yu. "Comparison of three SVPWM strategies." Journal of electronic science and technology of china 5.3 (2007): 283-287.

[21] Kumar, K. Vinoth, et al. "Simulation and comparison of SPWM and SVPWM control for three phase inverter." ARPN Journal of Engineering and Applied Sciences 5.7 (2010): 61-74.

[22] Jung, Jin-Woo, Ph.d student, Project #2 Space Vector PWM Inverter, Mechatronic Systems Laboratory Department of Electrical and Computer Engineering, The Ohio State University, 2005

[23] Anders Roland Pedersen, Cemre Yigen, John Andersen and Mikkel P. Ehmsen, Implementation and Control of an Induction Motor on a Go-cart, 8. Semester project, 2011